Infection and chronic disease activate a brain-muscle signaling axis that regulates muscle performance

Shuo Yang[1,*], Meijie Tian[2,*], Yulong Dai[3,4,5,*], Shengyong Feng[3,*], Yunyun Wang[6,*], Deepak Chhangani[7], Tiffany Ou[1], Wenle Li[8], Ze Yang[9], Jennifer McAdow[1], Diego E. Rincon-Limas[7], Xin Yin[5,#], Wanbo Tai[3,4,#], Gong Cheng[3,4,#], and Aaron Johnson[1,10,#]

[1]Department of Developmental Biology, Washington University School of Medicine in St. Louis, St. Louis, MO 63110, USA.

[2]Genetics Branch, Oncogenomics Section, National Cancer Institute, NIH, Bethesda, MD 20892, USA

[3]Tsinghua-Peking Center for Life Sciences, School of Medicine, Tsinghua University, Beijing 100084, China.

[4]Institute of Infectious Diseases, Shenzhen Bay Laboratory, Shenzhen, Guangdong, China

[5]State Key Laboratory of Veterinary Biotechnology, Harbin Veterinary Research Institute, Chinese Academy of Agricultural Sciences, Harbin 150069, P.R. China.

[6]Tongji Medical College of Huazhong University of Science and Technology, Department of Forensic Medicine, Wuhan, Hubei 430074, China

[7]Department of Neurology, College of Medicine, University of Florida, Gainesville, FL 32610, USA

[8]State Key Laboratory of Molecular Vaccinology and Molecular Diagnostics & Center for Molecular Imaging and Translational Medicine, School of Public Health, Xiamen University, Xiamen, Fujian 361005, China.

[9]The Key Laboratory of Marine Genetics and Breeding, College of Marine Life Sciences, Ocean University of China, Qingdao 266100, China

[10]Lead corresponding author

[*]These authors contribute equally to this manuscript

[#]Authors for correspondence:
yinxin@caas.cn(Y.Y)
taiwb@szbl.ac.cn(W.T)
gongcheng@mail.tsinghua.edu.cn(G.C)
anjohnson@wustl.edu(A.J)

Graphic abstract

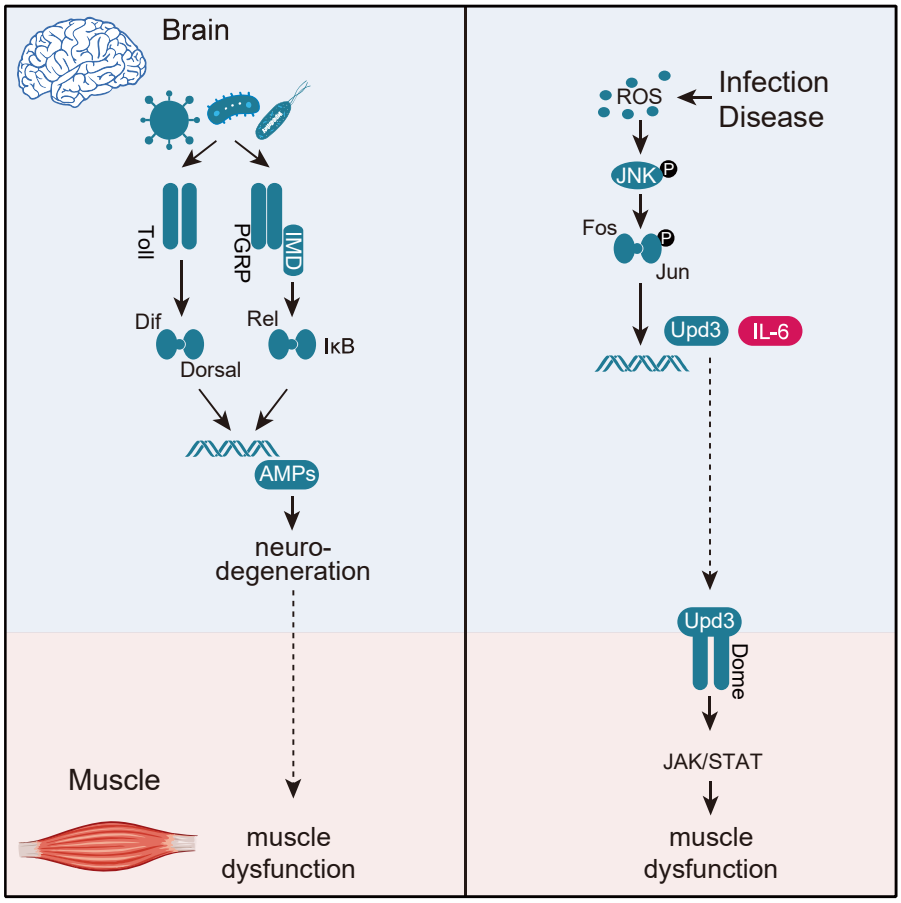

Summary

Infections and neurodegenerative diseases induce neuroinflammation, but affected individuals often show a number of non-neural symptoms including muscle pain and muscle fatigue. The molecular pathways by which neuroinflammation causes pathologies outside the central nervous system (CNS) are poorly understood, so we developed three models to investigate the impact of neuroinflammation on muscle performance. We found that bacterial infection, COVID-like viral infection, and expression of a neurotoxic protein associated with Alzheimer′s disease promoted the accumulation of reactive oxygen species (ROS) in the brain. Excessive ROS induces the expression of the cytokine Unpaired 3 (Upd3) in insects, or its orthologue IL-6 in mammals, and CNS-derived Upd3/IL-6 activates the JAK/Stat pathway in skeletal muscle. In response to JAK/Stat signaling, mitochondrial function is impaired and muscle performance is reduced. Our work uncovers a brain-muscle signaling axis in which infections and chronic diseases induce cytokine-dependent changes in muscle performance, suggesting IL-6 could be a therapeutic target to treat muscle weakness caused by neuroinflammation.

Introduction

Neuroinflammation refers to the activation of innate immune pathways in the central nervous system (CNS). Infectious diseases, including meningitis, Zika fever, and COVID-19, chronic conditions including Alzheimer's disease and Parkinson's Disease, and normal aging all induce neuroinflammation (Farmen et al., 2021; Frere et al., 2022; Hou et al., 2019; Leng and Edison, 2021; Lum et al., 2017). Although neuroinflammation can be activated by a number of factors, the inflammatory pathways appear to converge on a common disease mechanism that initiates neurodegeneration, defined as the disruption of neural function through changes in neuronal structure or survivability (Glass et al., 2010; Ransohoff, 2016). Symptoms associated with neurodegeneration are wide spread and include anxiety, insomnia, muscle weakness and even paralysis (Cao et al., 2013; Jayaraman et al., 2021; Leng and Edison, 2021). Neuroinflammation and neurodegeneration are thought to primarily target cells in the CNS, and symptoms in tissues outside of the CNS are due to changes in direct neural connectivity or function with a target tissue. However, neuroinflammation may also alter the secretome of the CNS, which could have profound effects on organ physiology outside of the CNS.

Inter-organ communication is emerging as a fundamental mechanism regulating whole-body physiology and homeostasis. Organs communicate using secreted molecules that enter circulation, translocate to target tissues, and then direct a variety of processes including immunity, behavior, neurogenesis, cardiovascular function, and cellular aging (Cai et al., 2021; Cao et al., 2022; Lee et al., 2014; Leiter et al., 2022; Robles-Murguia et al., 2020; Yang et al., 2019). Over 60 years ago it was proposed that skeletal muscle contractions liberate unknown factors that regulate metabolism (Goldstein, 1961). The discovery 40 years later that the cytokine IL-6 is released from skeletal muscle during exercise to regulate metabolism showed skeletal muscle is in fact an endocrine organ, which sparked great interest in understanding the role of muscle-derived signaling molecules, or myokines, on non-muscle physiology (Whitham and Febbraio, 2016). The CNS is a well-defined target of myokines, and over fifty muscle-derived proteins have been found to translocate from muscle to the brain (Droujinine et al., 2021). Myokines are now recognized as a heterogenous collection of proteins, that include conventional signaling molecules such as Bone Morphogenetic Proteins,

as well as signaling accessory proteins such as transporters, that induce a variety of responses including the proliferation of neural precursors and the synthesis of neurotransmitters (Leiter et al., 2022; Robles-Murguia et al., 2020). Although the muscle-brain signaling axis has well defined roles in regulating neural activity, it remains unclear if a complementary brain-muscle signaling axis regulates muscle function.

IL-6 is a highly conserved extracellular ligand that activates the JAK/Stat pathway. JAK/Stat signaling fulfills a diverse array of developmental processes and homeostatic responses in insects and mammals, and the *Drosophila* genome encodes three IL-6 related ligands, Unpaired 1 (Upd1), Upd2, and Upd3 (Johnson et al., 2011; Moresi et al., 2019; Villarino et al., 2017). Upon binding to the receptor Domeless (Dome), Upd ligands activate the JAK/Stat pathway (Brown et al., 2001; Fisher et al., 2016). While JAK/Stat signaling is essential for development, regeneration, and immune responses, inappropriate JAK/Stat signaling activity can disrupt normal mitochondrial function in *Drosophila* skeletal muscle and in cultured mammalian muscle cells (Abid et al., 2020; Agaisse and Perrimon, 2004; Ding et al., 2021; Shen et al., 2022). In mice, IL-6 activated JAK/Stat signaling contributes to sepsis-induced muscle atrophy and weakness, and IL-6 serum levels in patients have been inversely correlated with functional muscle outcomes (Custodero et al., 2020; Grosicki et al., 2020). In addition, JAK/Stat inhibitors can improve muscle function in patients with Critical illness myopathy and other inflammation conditions (Addinsall et al., 2021; Chen et al., 2021b; Zanders et al., 2022). These data argue that tight regulation of JAK/Stat signaling is essential to maintain proper muscle function.

Over the past several years the power of *Drosophila* to characterize inter-organ communication pathways (Rai et al., 2021; Robles-Murguia et al., 2020; Yang et al., 2019), and to identify pathogenic mechanisms driving infectious disease (Adamson et al., 2011; Chan et al., 2009; Hao et al., 2008; Harsh et al., 2020; Hughes et al., 2012; Liu et al., 2018; Yang et al., 2018) has come to light. We used *Drosophila* to investigate a putative brain-muscle signaling, and found neuroinflammation activates the brain-muscle axis and regulates muscle performance. By testing three models of neuroinflammation, that included *E. coli* infection in the brain, expression of a SARS-CoV-2 protein in the CNS, and expression of a neurotoxic amyloid-β protein associated with Alzheimer's disease (AD) in the CNS, we uncovered a general

mechanism in which Upd3 is expressed in the CNS in response to neuroinflammation, and subsequent JAK/Stat signaling in skeletal muscle disrupts mitochondrial function and reduces muscle performance. Incredibly, expressing SARS-CoV-2 proteins in the mouse brain also activated IL-6 expression, and reduced muscle performance. Long-COVID refers to a condition in which symptoms such as insomnia, muscle pain, and muscle fatigue persist after the SARS-CoV-2 virus is cleared from the respiratory tract (Subramanian et al., 2022; Xu et al., 2022). Bacterial infections in the CNS and AD are also associated with impaired muscle function (Beeri et al., 2021; Giannos et al., 2022; Martellosio et al., 2020). Our study argues neuroinflammation associated with bacterial infections, Long-COVID, and AD activates a conserved, IL-6 mediated brain-muscle signaling axis, suggesting IL-6 could be a therapeutic target for patients with infections and chronic diseases.

Results

Neural infection disrupts mitochondrial function in skeletal muscle

Neuroinflammation refers to the activation of innate immune pathways in the CNS, and bacterial infection in the *Drosophila* brain activates the innate immune response and impairs muscle function (Cao et al., 2013). To identify the pathways by which neuroinflammation affects muscle performance, we validated a neural infection model that uses direct infection of non-pathogenic *E. coli* to infect the fly brain and induce neuroinflammation. Infected animals had a significant reduction in climbing capacity compared to vehicle-injected controls at two- and six-days post-infection (Fig. 1A,B). The survival rate of infected flies was comparable to controls (Fig. S1A). Importantly, bacteria injected into the brain did not infect skeletal muscle (Fig. S1B), arguing the neural infection model induced neuroinflammation and impaired muscle performance without affecting survival or causing secondary infections in muscle. Muscle weakness could be caused by a number of factors, and we found flight muscle myofiber morphology was largely normal in infected animals but skeletal muscle mitochondrial activity was significantly reduced (Figs. 1C,D, S1C). Thus, infection-induced neuroinflammation disrupts mitochondrial function in skeletal muscle.

To understand if neuroinflammation acts through the innate immune pathways to disrupt skeletal muscle function, we used our previously developed genetic model to activate the innate response in the CNS and assay muscle performance. In *Drosophila*, *E. coli* infection activates the Peptidoglycan receptor proteins (PGRPs) of the Immune Deficiency (IMD) pathway, which initiates the expression of antimicrobial peptides (AMPs) (Fig. 1E). AMPs in turn induce neurodegeneration, and inhibit climbing capacity (Cao et al., 2013). Transgenic expression of the PGRP-LC or the PGRP-LE receptor activates the IMD pathway in the absence of infection (Fig. S1D)(Yang et al., 2019), and we found flies that expressed PGRP-LC or PGRP-LE in the CNS showed significantly reduced climbing capacity compared to age matched controls (Fig. 1F). Similar to the bacterial infection model, myofiber morphology was unaffected in PGRP expressing flies, but surprisingly skeletal muscle mitochondrial activity was also unaffected (Figs. 1G,H, S1E). Bacterial infection therefore activates two pathways that impact muscle performance. An IMD-dependent pathway disrupts skeletal muscle performance but not mitochondrial activity, and an IMD-independent pathway regulates

118 mitochondrial activity in skeletal muscle.

119 **Neural infection activates the brain-muscle signaling axis to regulate mitochondrial**
120 **activity**

121 Our studies of innate immune pathways showed inflammation-induced neurodegenera-
122 tion does not regulate mitochondrial activity in skeletal muscle, raising the possibility that
123 neuroinflammation activates a second mechanism that regulates muscle performance (Fig.
124 1I). Bacterial infection can alter the secretome of the infected tissue, and secreted proteins
125 are often used for inter-organ communication (Cai et al., 2021). Infection outside the CNS
126 induces *upd3* expression, and Upd3 is a secreted signaling ligand that activates the Janus
127 kinase/signal transducer and activator of transcription (JAK/Stat) pathway (Sanchez Bosch et
128 al., 2019). In addition, the JAK/Stat pathway regulates mitochondrial activity in *Drosophila*
129 skeletal muscle and in cultured mammalian muscle cells (Abid et al., 2020; Ding et al., 2021).
130 We hypothesized that bacteria-induced neuroinflammation releases Upd3 into circulation,
131 which activates the JAK/Stat pathway in skeletal muscle and modulates mitochondrial func-
132 tion. Bacterial infection enriched *upd3* expression in the brain (Fig. 2A), and enhanced
133 expression of the JAK/Stat target gene *socs36E* in skeletal muscle (Fig. 2A). However, *upd3*
134 expression was unaffected in flies that expressed PGRP-LC or PGRP-LE in the CNS (Fig.
135 S2A). The JAK/Stat pathway activates the transcription factor Stat92E, and *10XStat92E.GFP*
136 is a validated reporter of Stat92E activity (Bach et al., 2007). *10XStat92E.GFP* expression in
137 skeletal muscle was unaffected in flies that expressed PGRP-LC (Fig. S2B). These results
138 argue the JAK/Stat pathway and innate immune pathways are independently activated in
139 response to bacterial infection.

140 To understand if JAK/Stat signaling can modulate muscle performance, we overex-
141 pressed Upd3 in the CNS with *elav.Gal4*, and found *elav>upd3* flies had significantly reduced
142 climbing ability (Fig. 2B,C). Since *elav.Gal4* is active in the embryo and can impede growth
143 (Fig. S2C,D), we used the inducible gene-switch system (*elav^{GS}.Gal4*) to activate *upd3* ex-
144 pression in the CNS of adult flies (hereafter, Upd3 gene switch). Upd3 gene switch flies
145 showed enhanced *socs36E* expression in skeletal muscle, and reduced climbing capacity
146 (Fig. 2D-F). Strikingly, mitochondrial activity in skeletal muscle was significantly reduced in
147 Upd3 gene switch flies even though myofiber morphology was normal (Figs. 2G,H S2E).

148 These studies support the model that bacteria-induced neuroinflammation releases Upd3 into
149 circulation, which in turn activates the JAK/Stat pathway in skeletal muscle to modulate mi-
150 tochondrial function. To functionally test our model, we knocked down *upd3* in the CNS and
151 found *upd3* knock down mitigated climbing defects associated with bacterial infection. Simi-
152 larly, knocking down the Upd3 receptor *domeless* in skeletal muscle improved muscle
153 performance in infected flies (Figs. 2I, S2F). *upd3* knock down in the CNS also improved
154 muscle mitochondrial function in infected flies (Fig. 2J,K). Our data argue that bacterial infec-
155 tion activates a brain-muscle signaling axis in which CNS-derived Upd3 modulates
156 mitochondrial activity in skeletal muscle.

157 **A viral model of neuroinflammation**

158 Activating the brain-muscle axis could be a specific response that is limited to bacterial
159 infection, or the brain-muscle axis could be activated in response to other pathogens that
160 infect the CNS. To distinguish between these possibilities, we aimed to develop a clinically
161 relevant model of viral infection in the CNS. A common symptom of COVID-19 is neuroin-
162 flammation, and the SARS-CoV-2 protein ORF3a activates the innate immune response
163 (Crunfli et al., 2022; Frere et al., 2022; Song et al., 2021; Yang et al., 2021; Zhang et al.,
164 2022). We asked if ORF3a protein is present in the brain of SARS-CoV-2 patients on autopsy,
165 and, in the cerebellum, we detected ORF3a in the plasmalemma and cytolymph of Purkinje
166 cells and in Granular cells of (Fig. 3A-C). ORF3a was also present in pyramidal cells of the
167 hippocampus (Fig. 3C). ORF3a was not identified in samples from uninfected patients (Fig.
168 3C). Our studies argue ORF3a is neuroinvasive and could directly induce neuroinflammation,
169 and align with recent observations showing SARS-CoV-2 can infect astrocytes in the brain
170 and individual SARS-CoV-2 proteins, such as Spike protein, have been detected after the
171 viral infection is cleared (Crunfli et al., 2022; Swank et al., 2022). ORF3a expression can
172 therefore be used as a clinically relevant model of viral infection in the CNS.

173 **ORF3a reduces muscle performance**

174 We used the UAS-Gal4 system to express ORF3a in the *Drosophila* CNS (*elav>ORF3a)*,
175 and found ORF3a expression alone was sufficient to activate neuroinflammation and reduce
176 muscle performance (Fig. 4A-C). The life span of *elav>ORF3a* flies was also reduced (Fig.
177 S3A). Similar to our bacterial infection model, skeletal muscle morphology was unaffected in

178 *elav>ORF3a* flies (Fig. S3B). Interestingly, muscle performance and longevity were not af-
179 fected in flies that expressed ORF3a in muscle, suggesting ORF3a acts cell
180 non-autonomously to regulate muscle physiology (Fig. S3C,D).

181 **ORF3a causes Long-COVID like symptoms**

182 Long-COVID refers to ongoing clinical symptoms, including memory loss, anxiety, in-
183 somnia, muscle weakness, and fatigue, after SARS-CoV-2 infection is no longer detectable in
184 the respiratory tract (Huang et al., 2021; Taquet et al., 2021). Persistent neuroinflammation is
185 observed in post-infectious patients and might be a major cause of Long-COVID. ORF3a
186 expressing flies showed neuroinflammation, muscle weakness, and fatigue and we asked if
187 ORF3a expression caused any additional Long-COVID like symptoms. Insomnia is a symp-
188 tom associated with Long-COVID (Thompson et al., 2022), and locomotor activity can be
189 used to study circadian rhythms and sleep parameters in *Drosophila* (Chiu et al., 2010;
190 Seugnet et al., 2009). Flies that expressed ORF3a in the CNS showed insomnia-like pheno-
191 type at night, but animals that expressed ORF3a in glia showed normal circadian behavior
192 (Fig. S3E-H). These data highlight the possibility that Long-COVID like symptoms, including
193 neuroinflammation, insomnia, and muscle weakness, could be caused by the persisting
194 presence of ORF3a, and other SARS-CoV-2 proteins, after the SARS-CoV-2 virus has been
195 cleared. In addition, our studies argue ORF3a expression can used to model Long-COVID like
196 symptoms.

197 **ORF3a activates innate immune pathways and the brain-muscle signaling axis**

198 The mechanism by which ORF3a affects skeletal muscle performance could mimic that
199 of *E. coli* infection in which neuroinflammation initiates AMP-mediated neurodegeneration via
200 the innate immune pathways, and concurrently activates the Upd3-mediated brain-muscle
201 signaling axis. We used enhancer-suppressor studies to test the possibility that
202 ORF3a-mediated activation of the innate immune pathways regulates muscle performance
203 and longevity, and found mutations in components of the IMD and the Toll pathways sup-
204 pressed the *elav>ORF3a* phenotypes (Fig. 4D). The Toll and IMD pathways can also initiate
205 AMP-mediated cell death (Cao et al., 2013), and flies that expressed ORF3a in the CNS
206 showed elevated apoptosis in the brain (Fig. 4E). We inhibited apoptosis in *elav>ORF3a* flies
207 by co-expressing p35, and found muscle performance was improved and life span was ex-

208 tended (Figs. 4D, Fig. S3I). These data suggest ORF3a activates an innate immune re-
209 sponse that promotes neurodegeneration and reduces muscle performance.

210 To understand if ORF3a also activates the Upd3-mediated brain-muscle signaling axis,
211 we used the inducible gene-switch system to express ORF3a in the adult CNS, and found
212 ORF3a gene switch flies had reduced climbing capacity (Fig. 4F). Importantly, ORF3a gene
213 switch flies also showed reduced mitochondrial activity in skeletal muscle, which is a pheno-
214 type specific to Upd3 overexpression (Fig. 4G,H). Flies that expressed ORF3a in the CNS
215 showed enriched *upd3* expression in the brain, and enriched *socs36E* expression in skeletal
216 muscle (Fig. 4I). Furthermore, *elav>ORF3a* flies showed a dramatic induction of
217 *10XStat92E.GFP* expression in skeletal muscle, arguing ORF3a expression in the CNS di-
218 rects a Stat92E transcriptional response in skeletal muscle (Fig. 4J). ORF3a therefore
219 regulates skeletal muscle performance by activating Upd3-mediated brain-muscle signaling
220 axis, and by initiating an innate immune response that promotes neurodegeneration.

221 **The brain-muscle axis is activated by ROS**

222 How then does persistent ORF3a expression activate the brain-muscle axis and induce
223 Long-COVID like symptoms? ROS production can induce Upd3/IL-6 expression across spe-
224 cies (Gera et al., 2022; Henriquez-Olguin et al., 2015; Santabarbara-Ruiz et al., 2015), so we
225 asked if ORF3a could also activate ROS production. HEK293 and HeLa cells transfected with
226 ORF3a showed significantly higher ROS levels than control transfected cells (Figs. S4A, B),
227 and *elav>ORF3a* flies had elevated ROS levels in the brain (Fig.5A). In addition, *elav>ORF3a*
228 flies treated with a ROS scavenger that reduces ROS levels showed improved muscle per-
229 formance compared to untreated controls (Fig.5B). ROS activates the JNK pathway to induce
230 Upd3 expression (Gera et al., 2022), and the levels of phosphorylated JNK were elevated in
231 *elav>ORF3a* flies (Fig.5C). Importantly, ROS production was unaffected in *elav>upd3* flies,
232 arguing Upd3 acts downstream of an ORF3a-ROS-JNK signaling cascade (Figs.5D).

233 Members of the nicotinamide adenine dinucleotide phosphate (NADPH) oxidase (NOX)
234 and dual oxidase (DUOX) family of proteins are the primary producers of cellular ROS and, in
235 response to bacterial and viral infections, NOX and DUOX derived ROS contribute to in-
236 flammation and tissue damage (Khomich et al., 2018; Lee et al., 2015). The mitochondrial
237 electronic transport chain (ETC) also generates ROS through a NOX and DUOX independent

238 mechanism (Zhao et al., 2019). The super oxidase dismutase (SOD) and catalase (CAT)
239 enzymes reduce ROS levels and detoxify the cellular environment in response to ROS pro-
240 duction (Fig.5E). To understand how SARS-CoV-2 infections might alter ROS levels, we
241 assayed *nox* and *duox* expression in the brain, but found *nox* and *duox* expression was un-
242 affected in *elav>ORF3a* flies (Fig.5F). A second possibility is that ORF3a reduces SOD and
243 CAT levels, which would increase ROS levels. However, the expression of *sod1, sod2,* and
244 *cat* in the brain was also unaffected in *elav>ORF3a* flies (Fig.5F).

245 We next considered the possibility that ORF3a activates ROS production through an
246 atypical mechanism. Viroporins are hydrophobic proteins encoded by some viruses that ag-
247 gregate in host cell membranes (Nieva et al., 2012). The influenza virus M2 protein is a
248 well-studied viroporin, and M2 functions as an ion channel that induces mitochondrial dys-
249 function and ROS production (Moriyama et al., 2019). ORF3a is also a viroporin, and
250 functions as a nonselective, Ca^{2+} permeable ion channel (Kern et al., 2021). Missense muta-
251 tions in residues positioned at the top of the polar cavity (Q57E) or at the of the base of the
252 hydrophilic grooves (S58L, Q116L) partially reduced ORF3a ion channel activity (Fig.5G)
253 (Kern et al., 2021). In addition, ORF3a proteins containing either the Q57E mutation or the
254 S58L, Q116L mutations partially attenuated ORF3a-induced cellular phenotypes (Chen et al.,
255 2021a). We hypothesized that ORF3a activates ROS production through its viroporin activity,
256 and generated a triple mutant that disrupts the polar cavity and the hydrophilic grooves
257 (Q57E/S58L/Q116L; hereafter ORF3a.QSQ). Cells transfected with wild-type ORF3a showed
258 a dramatic reduction in mitochondrial activity, whereas mitochondrial activity in cells trans-
259 fected with ORF3a.QSQ was largely normal (Fig.5H,I; Fig. S4C). These data argue ORF3a
260 ion channel activity contributes to mitochondrial pathogenicity, and suggest ORF3a induces
261 ROS production by disrupting ion homeostasis. ORF3a expression in the CNS therefore
262 regulates muscle performance by activating a ROS-JNK-Upd3-JAK/Stat signaling pathway
263 that impairs mitochondrial function in skeletal muscle.

264 **ORF3a affects muscle performance in mammals**

265 We wanted to understand if ORF3a could also induce neuroinflammation and disrupt
266 muscle performance in mammals. Although ORF3a induced IL-1β and IL-8 expression
267 through an NF-κB-dependent mechanism in human cell lines (Gowda et al., 2021), the

268 pathogenicity of ORF3a in mammals has not been assessed *in vivo*. Adeno-associated virus
269 (AAV) strategies to deliver SARS-CoV-2 coding sequences successfully showed the N pro-
270 tein promotes inflammation and can induce lung injuries in mice (Pan et al., 2021). We used a
271 similar strategy involving retro-orbital AAV injections to deliver ORF3a to the frontal cortex of
272 adult mice (Figs. 6A, S5A-C). ORF3a activated the expression of multiple cytokines, including
273 IL-1β, CXCL-15, and the mammalian orthologue of Upd3, IL-6 (Fig. 6B,C). ORF3a express-
274 ing mice also showed a transient reduction in bodyweight (Fig. 6D). Similar to our results in
275 *Drosophila*, ORF3a induced apoptosis and enhanced ROS production in the mammalian
276 CNS (Fig. 6E,F). Strikingly, ORF3a expressing mice showed significant fatigue during
277 treadmill running from four to sixteen days after AAV injection (Fig. 6G). In addition, ROS
278 levels were elevated in skeletal muscles of ORF3a-expressing mice, suggesting mitochon-
279 drial dysfunction impaired muscle function (Fig. 6H). These results argue ORF3a expression
280 in mice disrupts muscle performance, and suggest neuroinflammation activates the
281 brain-muscle axis in mammals.

282 **A neurotoxic protein associated with Alzheimer's disease activates the brain-muscle**
283 **axis**

284 Neuroinflammation can also be activated in the absence of infection. For example, Alz-
285 heimer's disease (AD) is a non-infectious disease, and patients with AD often show chronic
286 neuroinflammation, muscle weakness, and elevated ROS levels in the brain (Lai et al., 2017;
287 Suryadevara et al., 2020). We performed a meta-analysis of 12 studies that characterized
288 serum protein levels in a total of 585 AD patients and 439 healthy controls, and found AD
289 patients had higher levels of IL-6 than unaffected patients (Fig. S6A). These observations
290 suggested AD induces IL-6 expression and activates the brain-muscle signaling axis. Amy-
291 loid-β (Aβ42) is a neurotoxic protein involved in AD progression, and Aβ42 has been used to
292 model AD in worms, flies, and mice. To understand if AD-associated neuroinflammation ac-
293 tivates the brain-muscle axis, we expressed Aβ42 in the CNS of adult flies (hereafter AD flies).
294 AD flies showed significantly reduced muscle performance increased ROS levels in the brain
295 (Fig. 7A,B). Similar to ORF3a expressing flies, AD flies had reduced muscle mitochondrial
296 activity but normal myofiber morphology (Fig.7C,D; Fig.S6B)(Casas-Tinto et al., 2011). In
297 addition, AD flies showed elevated *upd3* expression in the brain, and increased *socs36E* ex-

298 pression in muscle (Fig. 7F). AD flies also showed enriched *10XSTAT92E.GFP* expression in
299 muscle (Fig. 7G,H). These data argue Aβ42-induced neuroinflammation activates the
300 brain-muscle signaling axis and disrupts muscle performance.

301 **Discussion**

302 We have shown that bacterial infections, the SARS-CoV-2 protein ORF3a, and the
303 neurotoxic protein Aβ42 promote ROS accumulation in the brain. Excessive ROS induces
304 Upd3 expression in insects, or IL-6 expression in mammals, and CNS-derived Upd3/IL-6 ac-
305 tivates the JAK/Stat pathway in skeletal muscle. Muscle performance and mitochondrial
306 activity are in turn reduced in response to JAK/Stat signaling. This is the first study to define a
307 brain-muscle signaling axis, and highlights circulating Upd3/IL-6 as a novel mechanism by
308 which the CNS communicates with skeletal muscle. Since infections and chronic diseases
309 induce cytokine-dependent changes in muscle performance, our work suggests IL-6 could be
310 a therapeutic target to treat muscle dysfunction caused by neuroinflammation.

311 Each of the models of neuroinflammation we developed or characterized has a clear
312 clinical counterpart. For example, meningitis is an infection-induced inflammation of the me-
313 ninges that is an important cause of mortality and morbidity in neonates and infants (Kim,
314 2010). The meninges act as a protective layer that surrounds the CNS, but gram-negative
315 bacterial infections of the meninges, such as *E. coli*, can penetrate the blood-brain barrier and
316 directly infect the CNS (Kim, 2008). Similar to our *Drosophila* model of bacterial-induced
317 neuroinflammation, *E. coli* induced neonatal meningitis in rodents induced the expression of
318 several cytokines, including the Upd3 orthologue IL-6 (Barichello et al., 2014), and inflam-
319 matory myopathies have been observed in patients recovering from meningeal infections
320 (Martellosio et al., 2020). The Upd3/IL-6 brain-muscle signaling axis may therefore be acti-
321 vated in patients with CNS infections.

322 A common clinical symptom of COVID-19 is neuroinflammation, which can be assayed in
323 the cerebrospinal fluid (CSF) of SARS-CoV-2 infected patients (Vanderheiden and Klein,
324 2022). There has been much debate as to whether COVID-19 related neuroinflammation is a
325 systemic response to viral infections outside the CNS, or a more direct response to viral in-
326 fection in the CNS (Crunfli et al., 2022; Song et al., 2021; Yang et al., 2021). A recent study in
327 non-human primates argues SARS-CoV-2 can infect neurons (Beckman et al.), which sup-
328 ports our findings that ORF3a was expressed in the brain of patients with COVID-19. While
329 our study does not reveal how SARS-CoV-2 proteins arrive in the CNS, our results argue
330 ORF3a is neuroinvasive and causes neuroinflammation in flies and mammals. The ORF3a

331 transgenic fly is thus a preclinical model of COVID-19 that does not require the biosafety level
332 precautions needed for working with the SARS-CoV-2 virus.

333 Mild SARS-CoV-2 infection in the respiratory system was recently shown to promote
334 neuroinflammation in the CSF, to enhance microglial reactivity, and to induce the loss of oli-
335 godendrocytes and myelinated axons in mice (Fernández-Castañeda et al., 2022).
336 SARS-CoV-2 also induced changes in brain structure, visible by longitudinal magnetic reso-
337 nance imaging in infected patients, and enhanced cognitive decline (Douaud et al., 2022).
338 Interestingly, mild respiratory SARS-CoV-2 infection caused IL-6 levels to be enriched in the
339 serum for several weeks post-infection (Fernández-Castañeda et al., 2022). It is possible that
340 the brain-muscle axis is activated by respiratory infections via the CSF, and continues to
341 signal long after the initial infection. Similar to respiratory infections, ORF3a expression in the
342 brain activated neuroinflammation and reduced cell survivability in the CNS, suggesting
343 neurodegeneration is a common pathology of COVID-19 regardless of the site of
344 SARS-CoV-2 infection or viral protein expression.

345 During the post-acute phase of COVID-19, a significant proportion of patients experience
346 symptoms outside the respiratory system, and this constellation of post-acute sequelae has
347 been termed Long-COVID (Ballering et al., 2022; Subramanian et al., 2022; Xu et al., 2022)
348 (Huang et al., 2021; Taquet et al., 2021). Cohort studies of COVID-19 patients documenting
349 non-respiratory symptoms from three to twelve months after acute infection identified an in-
350 creased incidence of neurologic disorders and somatic symptoms that include muscle pain
351 and fatigue (Ballering et al., 2022; Xu et al., 2022). SARS-CoV-2 proteins, such as Spike
352 protein, have been detected in circulation after the viral infection is cleared (Swank et al.,
353 2022). We found ORF3a is neuroinvasive and induces neurodegeneration and reduced
354 muscle function. Long-COVID symptoms could be caused by the persistent expression of
355 SARS-CoV-2 proteins, including ORF3a, after the acute phase of SARS-CoV-2 infection has
356 been cleared. By using ORF3a to model Long-COVID, we have found that SARS-CoV-2 pro-
357 teins can have local effects on the infected tissue and far reaching effects on whole-body
358 physiology. One underlying cause of Long-COVID could be the disruption of inter-organ
359 communication pathways by the long-term expression of SARS-CoV-2 proteins during the
360 post-acute phase of COVID-19. The Upd3/IL-6 brain-muscle signaling axis may therefore be

activated by SARS-CoV-2 during both the acute and post-acute phases of COVID-19.

Alzheimer's disease (AD) is a chronic neurodegenerative disorder that affects nearly six million people in the United States, and neuroinflammation is one factor that leads to AD pathology (Dhapola et al., 2021). AD also accelerates sarcopenia, which is the loss of skeletal muscle mass and function with aging (Beeri et al., 2021). Although the connections between AD and sarcopenia are poorly understood, AD and musculoskeletal aging are associated with an overlapping set of differentially expressed genes that regulate mitochondrial function (Giannos et al., 2022). In addition, skeletal muscle mitochondria from individuals in the early phases of AD showed reduced respiratory kinetics and poor control of mitochondria coupling (Morris et al., 2021). Chronic neuroinflammation in AD correlates with reduced mitochondrial function in skeletal muscle, and our in silico analysis argues circulating IL-6 levels are increased in AD patients. Upd3 expression was also enriched in the fly model of AD, suggesting the Upd3/IL-6 brain-muscle signaling axis may be active in AD patients

Our three disease models have identified IL-6 and Stat inhibitors as potential therapeutics for patients with CNS infections, COVID-19, and AD. In fact, we successfully mitigated the effects of CNS bacterial infections by inhibiting Upd3/IL-6 and the JAK/Stat pathway. The Stat inhibitor ruxolitinib is approved to treat alopecia, psoriasis, lymphoma, and myelofibrosis (Haq and Adnan, 2022). Myelofibrosis is defined a myeloproliferative neoplasm that is often correlated with variants in *JAK2* (Arber et al., 2016). Although musculoskeletal symptoms are not part of the myelofibrosis diagnostic criteria, myelofibrosis patients that received ruxolitinib showed significant improvement of muscle mass over a six-month longitudinal study (Lucijanic et al., 2021). These clinical results align with our overall model that IL-6 and Stat inhibitors could inhibit changes to muscle performance induced by the Upd3/IL-6 brain-muscle signaling axis, and prevent muscle atrophy associated with muscle disuse.

Evolution of the brain-muscle axis

Why then did the Upd3/IL-6 brain-muscle signaling axis evolve? Skeletal muscle comprises 45% of the total human body mass, and consumes 28% of the body's total energy at rest (Chen et al., 2021b; McClave and Snider, 2001b). The adult brain consumes 20% of the resting energy expenditure (McClave and Snider, 2001a). The brain-muscle axis might limit mitochondrial function in muscle to reduce energy consumption and redirect energy ex-

391 penditure toward the CNS for recovery after disease or injury-induced neuroinflammation.
392 The immune system also consumes extensive energy, and shifts from 11% total energy
393 consumption in a healthy adult to 43% energy consumption during infection (Straub, 2017).
394 The brain-muscle signaling axis may induce muscle weakness to redirect energy expenditure
395 toward the immune system to accelerate clearance of infections or to promote other immune
396 system functions necessary for recovery.

397 A second hypothesis is that the brain-muscle axis restricts muscle function to protect
398 skeletal muscle from contraction-induced injuries. Muscle strains are contraction-induced
399 injuries, and are the most common sports injury (Dueweke et al., 2017). While neuroinflam-
400 mation has not been associated with contraction-induced injuries, it is possible that CNS
401 infections and chronic diseases inadvertently cause hypercontracility and muscle strains. If
402 the brain-muscle axis reduces mitochondrial function in response to neuroinflammation, then
403 skeletal muscle would be protected from contraction-induced injury. Since four drugs target-
404 ing neuroinflammation are currently in clinical trials (Dhapola et al., 2021), it will important to
405 identify the positive effects of the brain-muscle signaling axis on CNS recovery, systemic
406 immunity, and the prevention of muscle injuries.

407 **Materials and methods**

408 ***Drosophila* genetics**

409 The wild-type flies used were w^{1118} (Bloomington Stock Center, 3605) unless specifically
410 mentioned, all flies were maintained on standard cornmeal fly food unless noted otherwise.
411 Flies were cultured at 25℃under a normal light/dark cycle, unless noted otherwise. The
412 *Drosophila* stocks used in this study are described in Flybase (http://flybase.org/) unless
413 specified.

414 The RNAi lines were *UAS-Upd3-RNAi* (Bloomington Stock Center, 32859) and
415 *UAS-Dome-RNAi* (Bloomington Stock Center, 34618). Gal4 line were *GS.elav-Gal4* (Bloom-
416 ington Stock Center, 43642), *GS.nSyb-Gal4* (Bloomington Stock Center, 80699),
417 *elav-Gal4,Sb/TM6b* (Dr. Helen McNeill, WUSM), $elav^{strong}$*-Gal4* (Bloomington Stock Center,
418 458), *elav-Gal4,UAS-sfCherry/Cyo;TM3/TM6b* (Bloomington Stock Center, 93287), *re-*
419 *po-Gal4* (Bloomington Stock Center, 7415), and *Mef2-Gal4* (Bloomington Stock Center,
420 50742). UAS lines were *UAS-ORF3a* (lab made), *UAS-Upd3* (Dr. Bruce Edgar, The Univer-
421 sity of Utah), *UAS-PGRP-LCa* (Bloomington Stock Center, 30917), *UAS-PGRP-LE*
422 (Bloomington Stock Center, 33054), *UAS-p35* (Bloomington Stock Center, 5072),
423 UAS-Abeta42 (PMID: 21389082). Mutant lines were imd^{1} (Bloomington Stock Center, 55711),
424 $dorsal^{1}$ (Bloomington Stock Center, 3236), dif^{1} (Bloomington Stock Center, 36559).
425 *10XStat92E-GFP* reporter line was used to analyze JAK/Stat pathway activation (Blooming-
426 ton Stock Center, 26197).

427 UAS-SARS-CoV-2-ORF3a transgenic flies were generated by PCR-mediated subcloning of
428 the SARS-CoV-2-ORF3a coding sequence (pDONR207-SARS-CoV-2 ORF3a, #141271,
429 Addgene) into pUASt-Attb (EcoRI/XbaI). ORF3a was amplified with Takara PrimerSTAR
430 PCR enzyme (R050B, Takara) using the following primers:

431 ORF3a-CDS-Forward-CGGAATTCATGGACCTGTTCATGAGAATCTT

432 ORF3a-CDS-Rerverse-GCTCTAGATTACAGTGGCACGGAGGTG

433 Plasmid DNA was injected and targeted to a C31 integration site (Bloomington Stock 24481,
434 Rainbow Transgenic Flies); stable insertions were identified by standard methods.

435 **Mice**

436 Mice protocols used in this study were approved by the Institutional Animal Care and Use

437 Committee of Tsinghua University and performed in accordance with their guidelines (ap-
438 proval number:22-CG1). The laboratory animal facility has been accredited by the
439 Association for Assessment and Accreditation of Laboratory Animal Care International.
440 Six-week-old C57BL/6 mice were purchased from Charles River. All animals were maintained
441 in a specific pathogen-free animal facility at Tsinghua University with a 12h light/dark cycle
442 and normal chow diet and water.

443 **Longevity and motor function assays**

444 1d old adult flies were collected and transferred to fresh food daily for both assays. For lon-
445 gevity analysis, the number of dead flies was recorded daily. Kaplan-Meier survival curves
446 were generated, and statistical analysis was performed using log-rank analysis (Prism9,
447 GraphPad Software). To assess motor function, climbing assays were performed as de-
448 scribed(Moore et al., 2018). Briefly, 15-20 flies were placed into empty vials (9.5 cm high,1.7
449 cm in diameter) with flat bottoms, the flies were forced to the bottom of a vial by firmly tapping
450 the vial against the bench surface. Eight seconds after the tap, the number of flies that
451 climbed up the walls of a vial above the 5-cm mark was recorded as positive.

452 To assess climbing speed, around 20 adult flies were transferred to a 100ml glass cylinder.
453 The cylinder was tapped rapidly for 4 times. After the final tap, fly movement was recorded by
454 a camera. Average climbing speed was calculated by speed=height/8s.

455 For mice treadmill assay, 6-week-old mice were familiarized with the treadmill environment
456 before experiment, and assayed by a six-channel motor-drive uphill treadmill (UGO Basile,
457 Varese, Italy) at the speed of 15 m/min for 5 min/day throughout the experiment. The grid
458 (3mm bars, placed 8mm apart.) attached to mouse assembly, delivers the light foot-shock
459 (1mA). Shock intensity and frequency were recorded.

460 **Circadian rhythm analysis**

461 To analyze the sleep patterns of flies expressing either ORF3a or a control LacZ transgene in
462 neuronal or glial cells, we used the *Drosophila* activity monitor (DAM) system (Trikinetics,
463 Waltham). For this, we counted the number of times flies cross infrared beams in a 7-day
464 period. Individual flies were gently inserted in capillary tubes (5mm) containing 5% sucrose
465 and 2% agar. These tubes were then loaded horizontally in DM2 Trikinetics monitors under
466 12-hour Light/12-hour Dark conditions at 25°C. Counts were recorded by DAMSystem 3.11.1

467 and subsequently scanned and binned into 1-min intervals using DAMFileScan 1.11. Acto-
468 grams were plotted using NIH's ImageJ plugin ActogramJ
469 (https://bene51.github.io/ActogramJ/). Total activities of at least 6 consecutive days were
470 plotted.

471 **Bacteria, virus, and infection**

472 Collect *E.coli* (LB medium, 37°C) at optimal status (OD_{600} = 0.6~0.8) by centrifuged at 6000 g
473 for 5min at room temperature, wash the bacteria with sterile PBS for three times, and then
474 dilute the bacteria pellet with PBS to OD_{600} = 200. Infection was performed as described by
475 using 0.0125 mm needles (Fine Science Tools, 2600210)(Cao et al., 2013). Flies were kept
476 at 29°C and flipped daily with standard fly food.

477 AdV-ORF3a was construed in Keda Biotech, 20ul $3x10^{10}$PFU/ml virus was delivered to
478 wildtype mice (C57BL/6) by retro-orbital injection.

479 **Reactive oxygen species detection**

480 H2DCFDA (Thermo Fisher, D399) was used for ROS detection. For total ROS, 5 fly heads
481 were ground in 100ul cold PBS, then centrifuged for 15min (13500g, 4 degrees). 50ul su-
482 pernatant was incubated with 150ul H2DCFDA working solution (14uM, in PBS) for 30 min at
483 37 degrees. Fluorescence was measured by BioTek Synergy H1 (Ex/Em: 488/525).

484 **N-acetyl-L-cysteine treatment**

485 1g N-acetyl-L-cysteine (NAC) was dissolved in 10mL water, the solution could be aliquoted
486 into 1 ml per EP tube and frozen or stored at -80 degrees. For larvae treatment, 4g common
487 fly food was mixed with 200ul 1x NAC solution, and incubated at 25 degrees for 2~2 days egg
488 laying. For adult treatment, 100ul of 0.5xNAC solution was dipped onto the surface of fresh
489 food in vials (diameter: 2 cm). The vials were then allowed to dry at room temperature for 6
490 hours. Female adult flies were cultured on this NAC food at 25 degree, and fresh food was
491 changed every day.

492 **Mifepristone (RU486) treatment**

493 In RU486-induced experiments, 20 adult female flies (2–4 days old) per vial were fed with
494 50ug/mL of RU486 (M8046, Sigma; stock solution is 10mg/mL in DMSO, dilute to working
495 solution with ethanol before use) for 6 days. 100ul working solution was added to the surface
496 of fresh food (2cm diameter) and evaporate overnight (room temperature, protect from light).

497 Flies were raised on RU486/buffer-contained food at 25 degrees, and fresh food was
498 changed every day.

499 **Plasmids**

500 pCMV-GFP-SARS-CoV-ORF3a was generated by recombining the SARS-CoV-2-ORF3a
501 coding sequence (pDONR207 SARS-CoV-2 ORF3aA, #141271, Addgene) into
502 pDEST-CMV-N-EGFP (#122842, Addgene). pCMV-EGFP-ORF3a-Q57E-S58L-Q116L was
503 constructed as described(Yang et al., 2022). Following primers were used:

504 Q57E-F: CTGCTGGCCGTGTTCGAGTCCGCCTCTAAGATC

505 Q57E-R:GATCTTAGAGGCGGACTCGAACACGGCCAGCAG

506 Q57E-S58L-F: CTGGCCGTGTTCGAGCTCGCCTCTAAGATCATC

507 Q57E-S58L-R: GATGATCTTAGAGGCGAGCTCGAACACGGCCAG

508 S116L-F: CTCTGGTGTACTTCCTGCTGAGCATCAACTTCGTGCG

509 S116L-R: CGCACGAAGTTGATGCTCAGCAGGAAGTACACCAGAG

510 **LysoTracker staining**

511 Hela cells were seeded in 6-well plates with cover slips and grown to 50% confluency at 37°C
512 with 5% CO_2 in Dulbecco's modified Eagle's medium (12430047, Invitrogen) supplemented
513 with 10% heat-inactivated FBS (A4766801, Invitrogen). Cells were then transfected with
514 1000ng DNA, using standard Lipofectamine 3000 protocol (L3000008, Invitrogen). 24h post
515 transfection, media was removed, and cells were incubated with 10 nM LysoTracker Red
516 DND-99 (L7528, Invitrogen) for 1h. Cells was washed with PBS for three times, mounted and
517 imaged with a Zeiss LSM800 confocal microscope.

518 **TMRE and phalloidin staining**

519 For TMRE staining of muscle, adult fly hemi-thoraces were dissected in S2 medium (without
520 serum), and incubated in TMRE staining solution (200 nm TMRE in S2 medium, T669,
521 Thermo Fisher Scientific) for 30 min at room temperature. For TMRE staining of cells, Hela
522 cells were seeded into 6-well-plate with a cover slip, and transfected with 1000ng
523 pCMV-GFP-ORF3a or pCMV-GFP-ORF3a-Q57H-S58L-Q116L for 24h. Cells were washed
524 with PBS and incubated with TMRE staining solution (50 nm TMRE in DMEM, without serum)
525 for 15 min at 37 degree. After staining, samples (muscle or cells) were washed with PBS for 5
526 times, and immediately imaged using a Zeiss LSM880 confocal microscope. TMRE intensity

527 was quantified using ImageJ software and normalized to corresponding control group. For
528 phalloidin staining, adult fly muscles were dissected in PBS, and fixed with 4% formaldehyde
529 for 12min, and tissue staining was performed as described (Yang et al., 2022). Alexa Fluor™
530 555 Phalloidin (1:40; A34055, Thermo Fisher Scientific) was used to visualize F-Actin. Tis-
531 sues were imaged with a Zeiss LSM800 confocal microscope.

532 **Immunohistochemistry**

533 For patient samples, single-blind immunohistochemical was performed by Wuhan Servicebio
534 technology with standard method as described (Watson and Soilleux, 2015), except an-
535 ti-SARS-CoV-2 ORF3a antibody was used (1:500; PA5-116946; Thermo Fisher Scientific).

536 **Western blotting**

537 To detect ORF3a and c-Caspase-3 expression, 10 adult female heads were homogenized in
538 200 ul IP buffer (20 mM Hepes, pH=7.4, 150 nM NaCl, 1% NP40, 1.5 mM MgCl2, 2 mM
539 EGTA, 10 mM NaF, 1 mM Na3VO4, 1X proteinase inhibitor). To detect 10XSTAT-GFP re-
540 porter expression, 8 adult thoraces (4 male and 4 female) were homogenized in 200ul IP
541 buffer. Samples were incubated on ice for 30 min and large debris was removed by 15min
542 centrifugation (12,000xg). Anti-cleaved-Caspase 3 (1:500; #9661, Cell Signaling Technology),
543 anti-SARS-CoV-2-ORF3a (1:250; 101AP, FabGennix International Inc), anti-Actin (1:500;
544 JLA20, DSHB), anti-beta-Tubulin (1:500; E7-C, DSHB), and anti-GFP (1:1000; TP-401, Tor-
545 rey Pines Biolabs) were used for immunoblotting. Western blots were performed by standard
546 method using precast gels (#456-1096, BioRad), and imaged with the ChemiDoc XRS+
547 system (BioRad).

548 **Cytokine protein measurements**

549 Samples were prepared with standard method as described (Sukoff Rizzo et al., 2012). Total
550 protein was determined by BCA Protein Assay Kit (23225, Thermo Scientific). Cytokines and
551 chemokines were analyzed for by Elisa (IL-1beta, ab197742, Abcam; CXCL-15, MOFI01258,
552 Assay Genie; IL-6, A12219, Yojanbio).

553 **Quantitative real-time RT-PCR**

554 Total RNA was extracted with TRIzol (15596026, Invitrogen), and quantitated with a
555 Nanodrop 2000 (Thermo Fisher). cDNA was prepared by reverse transcription with All-in-One
556 5X RT MasterMix (G592, Applied Biological Materials Inc) with 1000ng RNA. BlasTaq 2X

557 qPCR MasterMix (G891, Applied Biological Materials Inc) and ABI Step One system (Applied
558 Biosystems) were used for quantitative RT-PCR. Quantification was normalized to endoge-
559 nous ribosomal protein Rp32 mRNA or GAPDH mRNA. RT-PCR primers included:
560 Diptercin-F: GGCTTATCCGATGCCCGACG
561 Diptercin-R: TCTGTAGGTGTAGGTGCTTCCC
562 Attacin-A-F: ACGCCCGGAGTGAAGGATGTT
563 Attacin-A-R: GGGCGATGACCAGAGATTAGCAC
564 Drosomycin-F: GCAGATCAAGTACTTGTTCGCCC
565 Drosomycin-R: CTTCGCACCAGCACTTCAGACTGG
566 Metchnikowin-F: GACGCAACTTAATCTTGGAGCG
567 Metchnikowin-R: TTAATAAATTGGACCCGGTCTTGGTTGG
568 Eiger-F: AGCGGCGTATTGAGCTGGAG
569 Eiger-R: TCGTCGTCCGAGCTGTCAAC
570 4E-BP-F: GTTTGGTGCCTCCAGGAGTGG
571 4E-BP-R: CGTCCAGCGGAAAGTTTTCG
572 Mmp2-F: GAGATGCCCATTTCGATGCG
573 Mmp2-R: GCCGTACAACTGCTGAATGC
574 Duox-F: GCCCTGCTGCTTCTACTGAT
575 Duox-R: CGCTGTTTCTCGGTCTGACT
576 Nox-F: TCCGCAAGCTATTCCTGGAC
577 Nox-R: TTGCTCGGCAAAGTCCATCT
578 Sod1-F: TGCGTAATTAACGGCGATGC
579 Sod1-R: CATGCTCCTTGCCATACGGA
580 Sod2-F: CAAGTCGAAGAGCGACACCA
581 Sod2-R: TTGTTGGGCGAGAGGTTCTG
582 Cat-F: CAAAATGGCTGGACGCGATG
583 Cat-R: GGGAGGCATCCTTGATTCCA
584 Upd3-F: CCTGCCCCGTCTGAATCTCA
585 Upd3-R: TGAAGGCGCCCACGTAAATC
586 Socs36E-F: AGGAGGAGTTCCTCTTCTCGGTC

587 Socs36E-R: CGTGGCAGTCGAAGCTGAAC

588 CXCL-15-F: TCCAGAGCTTGAAGGTGTTGCC

589 CXCL-15-R: AACCAAGGGAGCTTCAGGGTCA

590 IL-6-F: CACAAGTCCGGAGAGGAGAC

591 IL-6-R: CAGAATTGCCATTGCACAAC

592 IL-18-F: GACCAAGTTCTCTTCGTTGACAA

593 IL-18-R: ACAGCCAGTCCTCTTACTTCA

594 IL-1beta-F: CGCAGCAGCACATCAACAAGAGC

595 IL-1beta-R: TGTCCTCATCCTGGAAGGTCCACG

596 TNF-F: CGTGGAACTGGCAGAAGAG

597 TNF-R: TGAGAAGAGGCTGAGACATAGG

598 ORF3a-F: CGCTACTGCAACGATACCGA

599 ORF3a-R: AACAGCAAGAAGTGCAACGC

600 **Ethics statement**

601 Research participants were enrolled at Wuhan Jinyintan Hospital of Huazhong University of
602 Science and Technology (HUST) through Human Investigation Committee Protocols,
603 KY-2020-15.0. The Institutional Review Board at HUST approved the protocols, and informed
604 consent was obtained from all participants. Postmortem COVID-19 brain tissues were ob-
605 tained from Department of Forensic Medicine Biobank of Tongji Medical college in HUST.
606 This study was supported by the Emergency Novel Coronavirus Pneumonia Project from the
607 Ministry of Science and Technology of China (2020YFC0844700).

608 **Bioinformatic and statistical analysis**

609 Protein structure was generated by Chimera1.16 (USCF). The AD meta analysis and Forest
610 Plot was generated with RevMan5 software. Comparisons of two samples were made using
611 Student's t-test, and multiple samples by one-way or two-way ANOVA. Survival curves were
612 compared using the Kaplan–Meier test. P values of less than 0.05 were considered statisti-
613 cally significant. All statistical analyses were performed with GraphPad Prism 9 software. The
614 sample sizes and number of replicates are indicated in the figure legends. Data collection and
615 data analysis were routinely performed by different authors to prevent potential bias. All indi-
616 viduals were included in data analysis.

617 **Acknowledgments**

618 We thank Dr. Bruce Edgar (The University of Utah) for the kind gift of *UAS-Upd3* stock; Dr.
619 Helen McNeill (WUSM) for providing stock of *elav-Gal4,Sb/TM6b*. We also thank Helen
620 McNeill and Mayssa Mokalled for critical reading of the manuscript. This work was funded by
621 grants from the National Institutes of Health (R01AR070299) to A.N.J.; the National Natural
622 Science Foundation of China (32188101, 81961160737, 31825001, 81730063, 8191101056,
623 82041006 and 31700148) to G.C.; the National Key Research and Development Plan of
624 China (2021YFC2300200, 2020YFC1200104, 2018YFA0507202) to G.C.; Tsinghua Univer-
625 sity Spring Breeze Fund (2020Z99CFG017), Shenzhen Science and Technology Project
626 (JSGG20191129144225464) to G.C.; Innovation Team Project of Yunnan Science and
627 Technology Department (202105AE160020) and the Yunnan Cheng Gong expert work-
628 station (202005AF150034) to G.C.; Natural Science Foundation of Heilongjiang Province
629 (JQ2021C005) to X.Y.; the National Institutes of Health (R01AG059871) to D.R..

630 **Author Contributions**

631 Conceptualization, S.Y., G.C., and A.J.; Methodology and Validation, S.Y., M.T, Y.D., D.C.,
632 D.R., and A.J.; Formal Analysis, S.Y., M.T, Y.D., S.F., Y.W., D.C., T.O., J.M., W.L., Z.Y., D.R.,
633 X.Y., W.T., G.C. and A.J.; Virtualization, S.Y., Z.Y., G.C., and A.J.; Investigation, S.Y., M.T,
634 Y.D., S.F., Y.W., and D.C.; Resources, D.R., X.Y., W.T., G.C. and A.J.; Writing Original Draft,
635 S.Y., X.Y., W.T., G.C. and A.J.; Review & Editing, S.Y., M.T, Y.D., S.F., Y.W., D.C., T.O.,
636 J.M., W.L., Z.Y., D.R., X.Y., W.T., G.C. and A.J.; Supervision, S.Y., X.Y., W.T., G.C. and A.J.;
637 Funding Acquisition, D.R., X.Y., G.C. and A.J..

638 **Competing interests**

639 The authors declare no competing interests.

640 **Data availability**

641 The data that support the findings of this study are available from the corresponding authors
642 upon request.

References

Abid, H., Ryan, Z.C., Delmotte, P., et al., 2020. Extramyocellular interleukin-6 influences skeletal muscle mitochondrial physiology through canonical JAK/STAT signaling pathways. FASEB journal : official publication of the Federation of American Societies for Experimental Biology 34, 14458-14472.

Adamson, A.L., Chohan, K., Swenson, J., et al., 2011. A Drosophila model for genetic analysis of influenza viral/host interactions. Genetics 189, 495-506.

Addinsall, A.B., Cacciani, N., Akkad, H., et al., 2021. JAK/STAT inhibition augments soleus muscle function in a rat model of critical illness myopathy via regulation of complement C3/3R. J Physiol 599, 2869-2886.

Agaisse, H., Perrimon, N., 2004. The roles of JAK/STAT signaling in Drosophila immune responses. Immunol Rev 198, 72-82.

Arber, D.A., Orazi, A., Hasserjian, R., et al., 2016. The 2016 revision to the World Health Organization classification of myeloid neoplasms and acute leukemia. Blood 127, 2391-2405.

Bach, E.A., Ekas, L.A., Ayala-Camargo, A., et al., 2007. GFP reporters detect the activation of the Drosophila JAK/STAT pathway in vivo. Gene Expr Patterns 7, 323-331.

Ballering, A.V., van Zon, S.K.R., Olde Hartman, T.C., et al., 2022. Persistence of somatic symptoms after COVID-19 in the Netherlands: an observational cohort study. Lancet (London, England) 400, 452-461.

Barichello, T., Dagostim, V.S., Generoso, J.S., et al., 2014. Neonatal Escherichia coli K1 meningitis causes learning and memory impairments in adulthood. Journal of neuroimmunology 272, 35-41.

Beckman, D., Bonillas, A., Diniz, G.B., et al., SARS-CoV-2 infects neurons and induces neuroinflammation in a non-human primate model of COVID-19. Cell Reports.

Beeri, M.S., Leugrans, S.E., Delbono, O., et al., 2021. Sarcopenia is associated with incident Alzheimer's dementia, mild cognitive impairment, and cognitive decline. Journal of the American Geriatrics Society 69, 1826-1835.

Brown, S., Hu, N., Hombria, J.C., 2001. Identification of the first invertebrate interleukin JAK/STAT receptor, the Drosophila gene domeless. Curr Biol 11, 1700-1705.

Cai, X.T., Li, H., Borch Jensen, M., et al., 2021. Gut cytokines modulate olfaction through metabolic reprogramming of glia. Nature 596, 97-102.

Cao, Y., Chtarbanova, S., Petersen, A.J., et al., 2013. Dnr1 mutations cause neurodegeneration in Drosophila by activating the innate immune response in the brain. Proceedings of the National Academy of Sciences of the United States of America 110, E1752-1760.

Cao, Y., Wang, Y., Zhou, Z., et al., 2022. Liver-heart cross-talk mediated by coagulation factor XI protects against heart failure. Science 377, 1399-1406.

Casas-Tinto, S., Zhang, Y., Sanchez-Garcia, J., et al., 2011. The ER stress factor XBP1s prevents amyloid-beta neurotoxicity. Hum Mol Genet 20, 2144-2160.

Chan, C.M., Tsoi, H., Chan, W.M., et al., 2009. The ion channel activity of the SARS-coronavirus 3a protein is linked to its pro-apoptotic function. Int J Biochem Cell Biol 41, 2232-2239.

Chen, D., Zheng, Q., Sun, L., et al., 2021a. ORF3a of SARS-CoV-2 promotes lysosomal exocytosis-mediated viral egress. Developmental cell 56, 3250-3263.e3255.

Chen, Z., Li, B., Zhan, R.Z., et al., 2021b. Exercise mimetics and JAK inhibition attenuate IFN-gamma-induced wasting in engineered human skeletal muscle. Sci Adv 7.

Chiu, J.C., Low, K.H., Pike, D.H., et al., 2010. Assaying locomotor activity to study circadian rhythms and sleep parameters in Drosophila. J Vis Exp.

Crunfli, F., Carregari, V.C., Veras, F.P., et al., 2022. Morphological, cellular, and molecular basis of brain infection in COVID-19 patients. Proc Natl Acad Sci U S A 119, e2200960119.

Custodero, C., Anton, S.D., Beavers, D.P., et al., 2020. The relationship between interleukin-6 levels and physical performance in mobility-limited older adults with chronic low-grade inflammation: The ENRGISE Pilot study. Arch Gerontol Geriatr 90, 104131.

Dhapola, R., Hota, S.S., Sarma, P., et al., 2021. Recent advances in molecular pathways and therapeutic implications targeting neuroinflammation for Alzheimer's disease. Inflammopharmacology 29, 1669-1681.

Ding, G., Xiang, X., Hu, Y., et al., 2021. Coordination of tumor growth and host wasting by tumor-derived Upd3. Cell Rep 36, 109553.

Douaud, G., Lee, S., Alfaro-Almagro, F., et al., 2022. SARS-CoV-2 is associated with changes in brain structure in UK Biobank. Nature 604, 697-707.

Droujinine, I.A., Meyer, A.S., Wang, D., et al., 2021. Proteomics of protein trafficking by in vivo tissue-specific labeling. Nature communications 12, 2382.

Dueweke, J.J., Awan, T.M., Mendias, C.L., 2017. Regeneration of Skeletal Muscle After Eccentric Injury. Journal of sport rehabilitation 26, 171-179.

Farmen, K., Tofino-Vian, M., Iovino, F., 2021. Neuronal Damage and Neuroinflammation, a Bridge Between Bacterial Meningitis and Neurodegenerative Diseases. Front Cell Neurosci 15, 680858.

Fernández-Castañeda, A., Lu, P., Geraghty, A.C., et al., 2022. Mild respiratory COVID can cause multi-lineage neural cell and myelin dysregulation. Cell 185, 2452-2468.e2416.

Fisher, K.H., Stec, W., Brown, S., et al., 2016. Mechanisms of JAK/STAT pathway negative regulation by the short coreceptor Eye Transformer/Latran. Mol Biol Cell 27, 434-441.

Frere, J.J., Serafini, R.A., Pryce, K.D., et al., 2022. SARS-CoV-2 infection in hamsters and humans results in lasting and unique systemic perturbations after recovery. Sci Transl Med 14, eabq3059.

Gera, J., Budakoti, P., Suhag, M., et al., 2022. Physiological ROS controls Upd3-dependent modeling of ECM to support cardiac function in Drosophila. Sci Adv 8, eabj4991.

Giannos, P., Prokopidis, K., Raleigh, S.M., et al., 2022. Altered mitochondrial microenvironment at the spotlight of musculoskeletal aging and Alzheimer's disease. Scientific reports 12, 11290.

Glass, C.K., Saijo, K., Winner, B., et al., 2010. Mechanisms Underlying Inflammation in Neurodegeneration. Cell 140, 918-934.

Goldstein, M.S., 1961. Humoral nature of the hypoglycemic factor of muscular work. Diabetes 10, 232-234.

Gowda, P., Patrick, S., Joshi, S.D., et al., 2021. Glycyrrhizin prevents SARS-CoV-2 S1 and Orf3a induced high mobility group box 1 (HMGB1) release and inhibits viral replication. Cytokine 142, 155496.

Grosicki, G.J., Barrett, B.B., Englund, D.A., et al., 2020. Circulating Interleukin-6 Is Associated with Skeletal Muscle Strength, Quality, and Functional Adaptation with Exercise Training in Mobility-Limited Older Adults. J Frailty Aging 9, 57-63.

Hao, L., Sakurai, A., Watanabe, T., et al., 2008. Drosophila RNAi screen identifies host genes important for influenza virus replication. Nature 454, 890-893.

Haq, M., Adnan, G., 2022. Ruxolitinib., StatPearls [Internet]. StatPearls Publishing, Treasure Island

(FL), p. https://http://www.ncbi.nlm.nih.gov/books/NBK570600/.

Harsh, S., Fu, Y., Kenney, E., et al., 2020. Zika virus non-structural protein NS4A restricts eye growth in Drosophila through regulation of JAK/STAT signaling. Dis Model Mech 13.

Henriquez-Olguin, C., Altamirano, F., Valladares, D., et al., 2015. Altered ROS production, NF-kappaB activation and interleukin-6 gene expression induced by electrical stimulation in dystrophic mdx skeletal muscle cells. Biochim Biophys Acta 1852, 1410-1419.

Hou, Y., Dan, X., Babbar, M., et al., 2019. Ageing as a risk factor for neurodegenerative disease. Nat Rev Neurol 15, 565-581.

Huang, C., Huang, L., Wang, Y., et al., 2021. 6-month consequences of COVID-19 in patients discharged from hospital: a cohort study. Lancet 397, 220-232.

Hughes, T.T., Allen, A.L., Bardin, J.E., et al., 2012. Drosophila as a genetic model for studying pathogenic human viruses. Virology 423, 1-5.

Igaki, T., Miura, M., 2014. The Drosophila TNF ortholog Eiger: emerging physiological roles and evolution of the TNF system. Seminars in immunology 26, 267-274.

Jayaraman, A., Htike, T.T., James, R., et al., 2021. TNF-mediated neuroinflammation is linked to neuronal necroptosis in Alzheimer's disease hippocampus. Acta Neuropathol Commun 9, 159.

Johnson, A.N., Mokalled, M.H., Haden, T.N., et al., 2011. JAK/Stat signaling regulates heart precursor diversification in Drosophila. Development 138, 4627-4638.

Kern, D.M., Sorum, B., Mali, S.S., et al., 2021. Cryo-EM structure of SARS-CoV-2 ORF3a in lipid nanodiscs. Nature structural & molecular biology 28, 573-582.

Khomich, O.A., Kochetkov, S.N., Bartosch, B., et al., 2018. Redox Biology of Respiratory Viral Infections. Viruses 10.

Kim, K.S., 2008. Mechanisms of microbial traversal of the blood–brain barrier. Nature Reviews Microbiology 6, 625-634.

Kim, K.S., 2010. Acute bacterial meningitis in infants and children. The Lancet Infectious Diseases 10, 32-42.

Lai, K.S.P., Liu, C.S., Rau, A., et al., 2017. Peripheral inflammatory markers in Alzheimer's disease: a systematic review and meta-analysis of 175 studies. J Neurol Neurosurg Psychiatry 88, 876-882.

Lee, J.H., Bassel-Duby, R., Olson, E.N., 2014. Heart- and muscle-derived signaling system dependent on MED13 and Wingless controls obesity in Drosophila. Proc Natl Acad Sci U S A 111, 9491-9496.

Lee, K.A., Kim, B., Bhin, J., et al., 2015. Bacterial uracil modulates Drosophila DUOX-dependent gut immunity via Hedgehog-induced signaling endosomes. Cell Host Microbe 17, 191-204.

Leiter, O., Zhuo, Z., Rust, R., et al., 2022. Selenium mediates exercise-induced adult neurogenesis and reverses learning deficits induced by hippocampal injury and aging. Cell Metab 34, 408-423.e408.

Leng, F., Edison, P., 2021. Neuroinflammation and microglial activation in Alzheimer disease: where do we go from here? Nat Rev Neurol 17, 157-172.

Liu, Y., Gordesky-Gold, B., Leney-Greene, M., et al., 2018. Inflammation-Induced, STING-Dependent Autophagy Restricts Zika Virus Infection in the Drosophila Brain. Cell Host Microbe 24, 57-68 e53.

Lucijanic, M., Galusic, D., Soric, E., et al., 2021. Ruxolitinib treatment improves muscle mass in patients with myelofibrosis. Annals of hematology 100, 1105-1106.

Lum, F.M., Low, D.K., Fan, Y., et al., 2017. Zika Virus Infects Human Fetal Brain Microglia and Induces Inflammation. Clin Infect Dis 64, 914-920.

Martellosio, J.P., Lauda-Maillen, M., Landron, C., et al., 2020. [Inflammatory myopathy following acute meningoccemia in a properdin-deficient patient: A case report]. La Revue de medecine interne 41, 46-49.

McClave, S.A., Snider, H.L., 2001a. Dissecting the energy needs of the body. Current Opinion in Clinical Nutrition & Metabolic Care 4, 143-147.

McClave, S.A., Snider, H.L., 2001b. Dissecting the energy needs of the body. Curr Opin Clin Nutr Metab Care 4, 143-147.

Moore, B.D., Martin, J., de Mena, L., et al., 2018. Short Abeta peptides attenuate Abeta42 toxicity in vivo. J Exp Med 215, 283-301.

Moresi, V., Adamo, S., Berghella, L., 2019. The JAK/STAT Pathway in Skeletal Muscle Pathophysiology. Front Physiol 10, 500.

Moriyama, M., Koshiba, T., Ichinohe, T., 2019. Influenza A virus M2 protein triggers mitochondrial DNA-mediated antiviral immune responses. Nat Commun 10, 4624.

Morris, J.K., McCoin, C.S., Fuller, K.N., et al., 2021. Mild Cognitive Impairment and Donepezil Impact Mitochondrial Respiratory Capacity in Skeletal Muscle. Function (Oxford, England) 2, zqab045.

Nieva, J.L., Madan, V., Carrasco, L., 2012. Viroporins: structure and biological functions. Nature reviews. Microbiology 10, 563-574.

Pan, P., Shen, M., Yu, Z., et al., 2021. SARS-CoV-2 N protein promotes NLRP3 inflammasome activation to induce hyperinflammation. Nat Commun 12, 4664.

Rai, M., Coleman, Z., Curley, M., et al., 2021. Proteasome stress in skeletal muscle mounts a long-range protective response that delays retinal and brain aging. Cell Metab 33, 1137-1154 e1139.

Ransohoff, R.M., 2016. How neuroinflammation contributes to neurodegeneration. Science (New York, N.Y.) 353, 777-783.

Robles-Murguia, M., Rao, D., Finkelstein, D., et al., 2020. Muscle-derived Dpp regulates feeding initiation via endocrine modulation of brain dopamine biosynthesis. Genes & development 34, 37-52.

Sanchez Bosch, P., Makhijani, K., Herboso, L., et al., 2019. Adult Drosophila Lack Hematopoiesis but Rely on a Blood Cell Reservoir at the Respiratory Epithelia to Relay Infection Signals to Surrounding Tissues. Developmental Cell 51, 787-803.e785.

Santabarbara-Ruiz, P., Lopez-Santillan, M., Martinez-Rodriguez, I., et al., 2015. ROS-Induced JNK and p38 Signaling Is Required for Unpaired Cytokine Activation during Drosophila Regeneration. PLoS Genet 11, e1005595.

Seugnet, L., Suzuki, Y., Thimgan, M., et al., 2009. Identifying sleep regulatory genes using a Drosophila model of insomnia. J Neurosci 29, 7148-7157.

Shen, R., Zheng, K., Zhou, Y., et al., 2022. A dRASSF-STRIPAK-Imd-JAK/STAT axis controls antiviral immune response in Drosophila. Cell Rep 40, 111143.

Song, E., Zhang, C., Israelow, B., et al., 2021. Neuroinvasion of SARS-CoV-2 in human and mouse brain. J Exp Med 218.

Straub, R.H., 2017. The brain and immune system prompt energy shortage in chronic inflammation and ageing. Nat Rev Rheumatol 13, 743-751.

Subramanian, A., Nirantharakumar, K., Hughes, S., et al., 2022. Symptoms and risk factors for long

COVID in non-hospitalized adults. Nature medicine 28, 1706-1714.
Sukoff Rizzo, S.J., Neal, S.J., Hughes, Z.A., et al., 2012. Evidence for sustained elevation of IL-6 in the CNS as a key contributor of depressive-like phenotypes. Transl Psychiatry 2, e199.
Suryadevara, V., Kluppel, M., Monte, F.D., et al., 2020. The Unraveling: Cardiac and Musculoskeletal Defects and Their Role in Common Alzheimer Disease Morbidity and Mortality. Am J Pathol 190, 1609-1621.
Swank, Z., Senussi, Y., Manickas-Hill, Z., et al., 2022. Persistent circulating SARS-CoV-2 spike is associated with post-acute COVID-19 sequelae. Clinical infectious diseases : an official publication of the Infectious Diseases Society of America.
Taquet, M., Geddes, J.R., Husain, M., et al., 2021. 6-month neurological and psychiatric outcomes in 236 379 survivors of COVID-19: a retrospective cohort study using electronic health records. Lancet Psychiatry 8, 416-427.
Thompson, E.J., Williams, D.M., Walker, A.J., et al., 2022. Long COVID burden and risk factors in 10 UK longitudinal studies and electronic health records. Nat Commun 13, 3528.
Vanderheiden, A., Klein, R.S., 2022. Neuroinflammation and COVID-19. Current opinion in neurobiology 76, 102608.
Villarino, A.V., Kanno, Y., O'Shea, J.J., 2017. Mechanisms and consequences of Jak-STAT signaling in the immune system. Nat Immunol 18, 374-384.
Watson, A.S., Soilleux, E.J., 2015. Detection of p62 on Paraffin Sections by Immunohistochemistry. Cold Spring Harb Protoc 2015, 756-760.
Whitham, M., Febbraio, M.A., 2016. The ever-expanding myokinome: discovery challenges and therapeutic implications. Nature Reviews Drug Discovery 15, 719-729.
Xu, E., Xie, Y., Al-Aly, Z., 2022. Long-term neurologic outcomes of COVID-19. Nature medicine.
Yang, A.C., Kern, F., Losada, P.M., et al., 2021. Dysregulation of brain and choroid plexus cell types in severe COVID-19. Nature 595, 565-571.
Yang, S., Yu, J., Fan, Z., et al., 2018. Bub1 Facilitates Virus Entry through Endocytosis in a Model of Drosophila Pathogenesis. J Virol 92.
Yang, S., Zhao, Y., Yu, J., et al., 2019. Sugar Alcohols of Polyol Pathway Serve as Alarmins to Mediate Local-Systemic Innate Immune Communication in Drosophila. Cell Host Microbe 26, 240-251 e248.
Zanders, L., Kny, M., Hahn, A., et al., 2022. Sepsis induces interleukin 6, gp130/JAK2/STAT3, and muscle wasting. J Cachexia Sarcopenia Muscle 13, 713-727.
Zhang, J., Ejikemeuwa, A., Gerzanich, V., et al., 2022. Understanding the Role of SARS-CoV-2 ORF3a in Viral Pathogenesis and COVID-19. Frontiers in microbiology 13, 854567.
Zhao, R.Z., Jiang, S., Zhang, L., et al., 2019. Mitochondrial electron transport chain, ROS generation and uncoupling (Review). Int J Mol Med 44, 3-15.

Figure 1. *E.coli* infection in the brain inhibits muscle performance

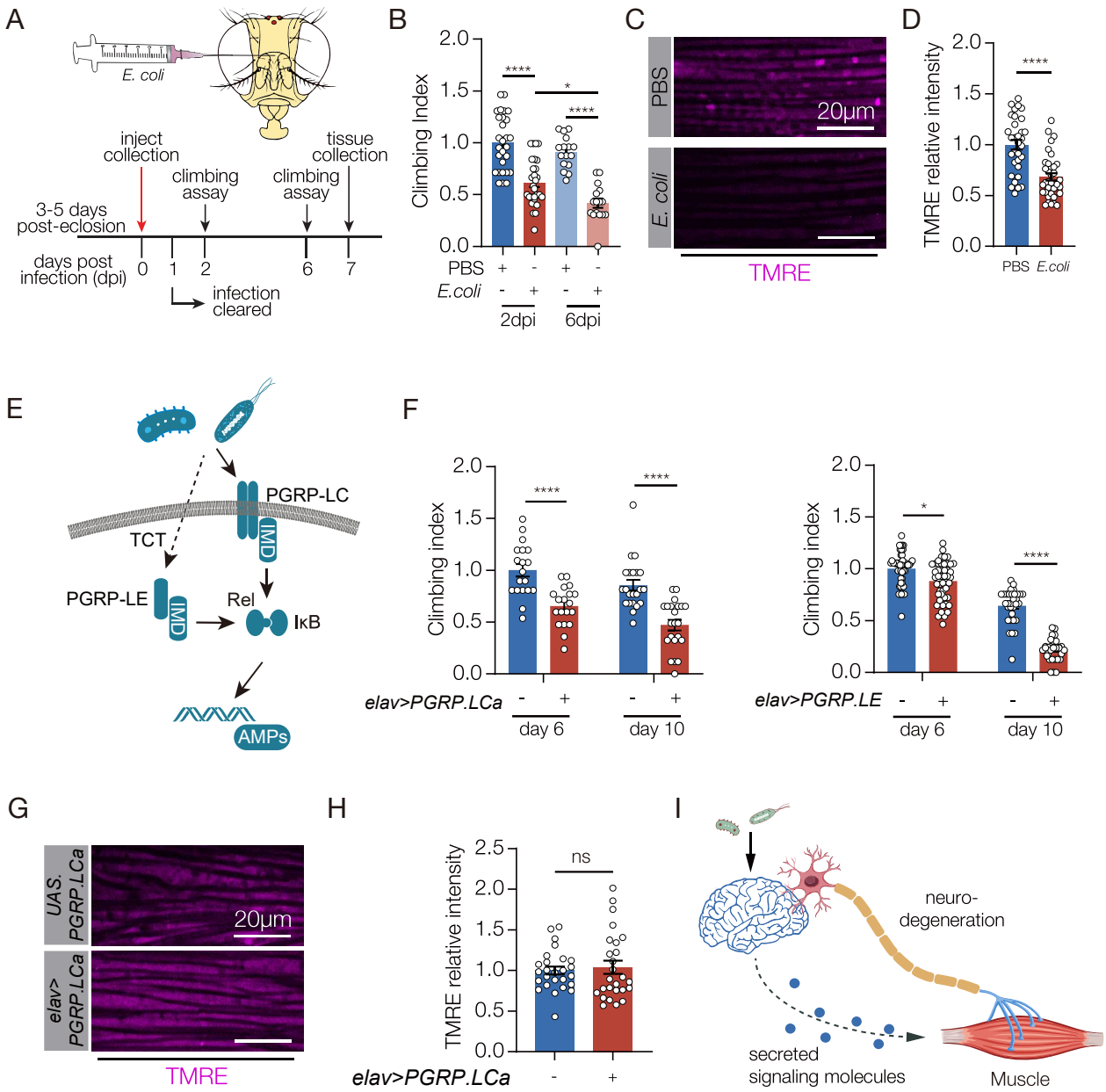

Figure 1. *E. coli* infection in the brain inhibits muscle performance. A. Experimental design to study the skeletal muscle response to *E. coli* infection in the brain. **B.** Climbing index. The climbing capacity of sterile-injected (PBS, control) and *E. coli* injected flies was determined at 2- and 6- days post injury (dpi). Infected flies showed reduced climbing capacity. **C.** Confocal micrographs of indirect flight muscles stained with the potentiometric dye tetramethyl rhodamine ethyl ester (TMRE; violet) to assess mitochondrial membrane potential. Muscles from sterile injected flies showed more TMRE staining than *E. coli* injected flies. **D.** Quantification of the TMRE signal shown in C. **E.** Diagram of Drosophila Immune Deficiency (IMD) pathway. Infectious pathogens activate the Peptidoglycan receptor proteins (PGRPs), which activate Relish (Rel) and i-κB, that in turn initiate expression of antimicrobial peptides (AMPs) **F.** Climbing indexes. The climbing capacity of flies that expressed PGRPs in the CNS under the control of *elav.Gal4* (*elav>PGRPLCa, elav>PGRPLE*) was reduced at 6- and 10-days after eclosion compared to controls (*UAS.PGRPLCa, UAS.PGRPLE*). **G.** Confocal micrographs of indirect flight muscles stained with TMRE (violet). **H.** Quantification of the TMRE signal shown in G. TMRE levels were comparable between *elav>PGRPLCa* flies and controls (*UAS.PGRPLCa*). **I.** Model depicting two possible communication pathways between brain and muscle. Significance was determined by two-way ANOVA (B, F), and two-sided unpaired Student's t-test (D, H). For climbing assays, data points represent the average of individual cohorts, with n≥15 flies per cohort. For TMRE, data points represent one of multiple fluorescent measurements per micrograph, with n≥5 flies per genotype. Error bars represent SEM. (*) $p < 0.05$, (**) $p < 0.01$, (***) $p < 0.001$, (****) $p < 0.0001$, (ns) non-significant.

Supplemental Figure 1, related to Figure 1

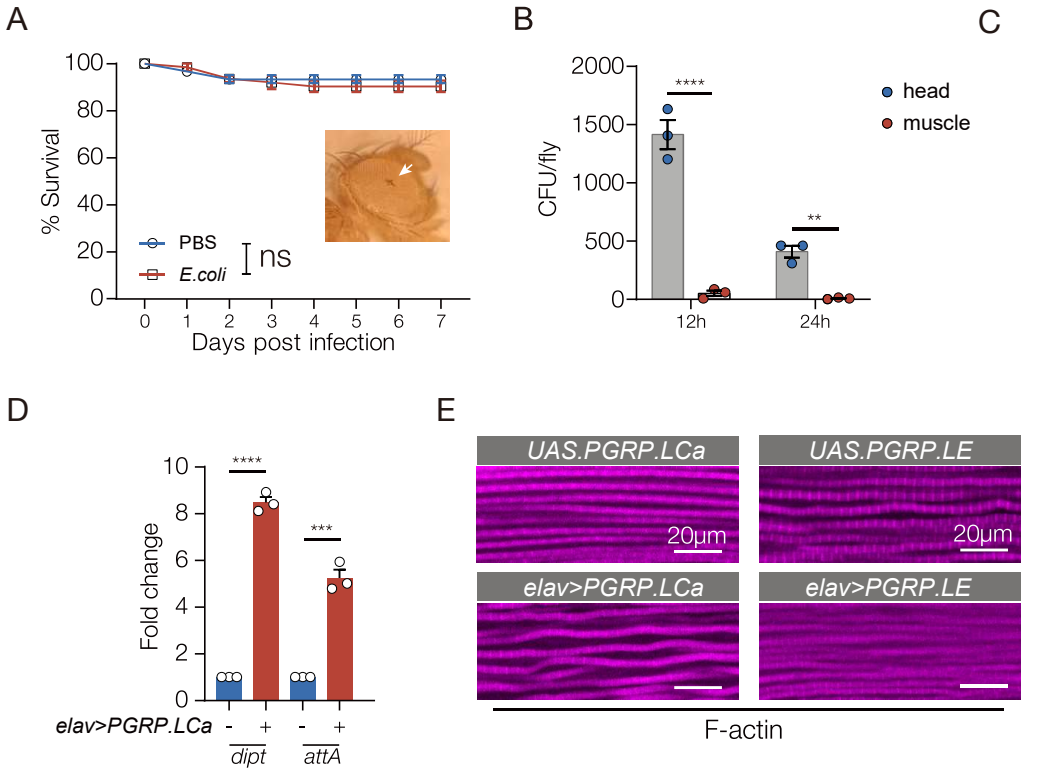

Figure S1. Related to Figure 1. A. Survival curve. Sterile-injected (PBS, control) and *E. coli* injected flies showed comparable longevity. White arrow shows the injection site. n=3 cohorts per genotype, with n≥20 flies per cohort. **B.** Colony forming unit (CFU) assay. Bacterial load in the brain dramatically decreased between 12- and 24- hours after *E. coli* injection. Muscle showed minimal bacterial infection. Each data point represents one biological replicate, with n=5 flies per replicate. **C.** Confocal micrographs of indirect flight muscle stained with phalloidin to visualize F-actin (violet). Muscle morphology was comparable between sterile-injected (PBS, control) and *E. coli* injected flies. **D.** qRT-PCR. Transcripts encoding the antimicrobial peptides *Dipt* and *attA* in the brain was enriched in *elav>PGRPLCa* flies compared to controls (*UAS.PGRPLCa*). Data points represent independent biological replicates, with n≥10 flies per cohort. **E.** Confocal micrographs of indirect flight muscle stained with phalloidin to visualize F-actin (violet). Muscle morphology was comparable among *elav>PGRPLCa* flies, *elav>PGRPLE* flies, and controls (*UAS.PGRPLCa, UAS.PGRPLE*). Significance was determined by Kaplan–Meier tests (A), or two-way ANOVA (B, D). Error bars represent SEM. (*) $p < 0.05$, (**) $p < 0.01$, (***) $p < 0.001$, (****) $p < 0.0001$, (ns) non-significant.

Figure 2. Neuroinflammation activates a Upd3 brain-muscle signaling axis.

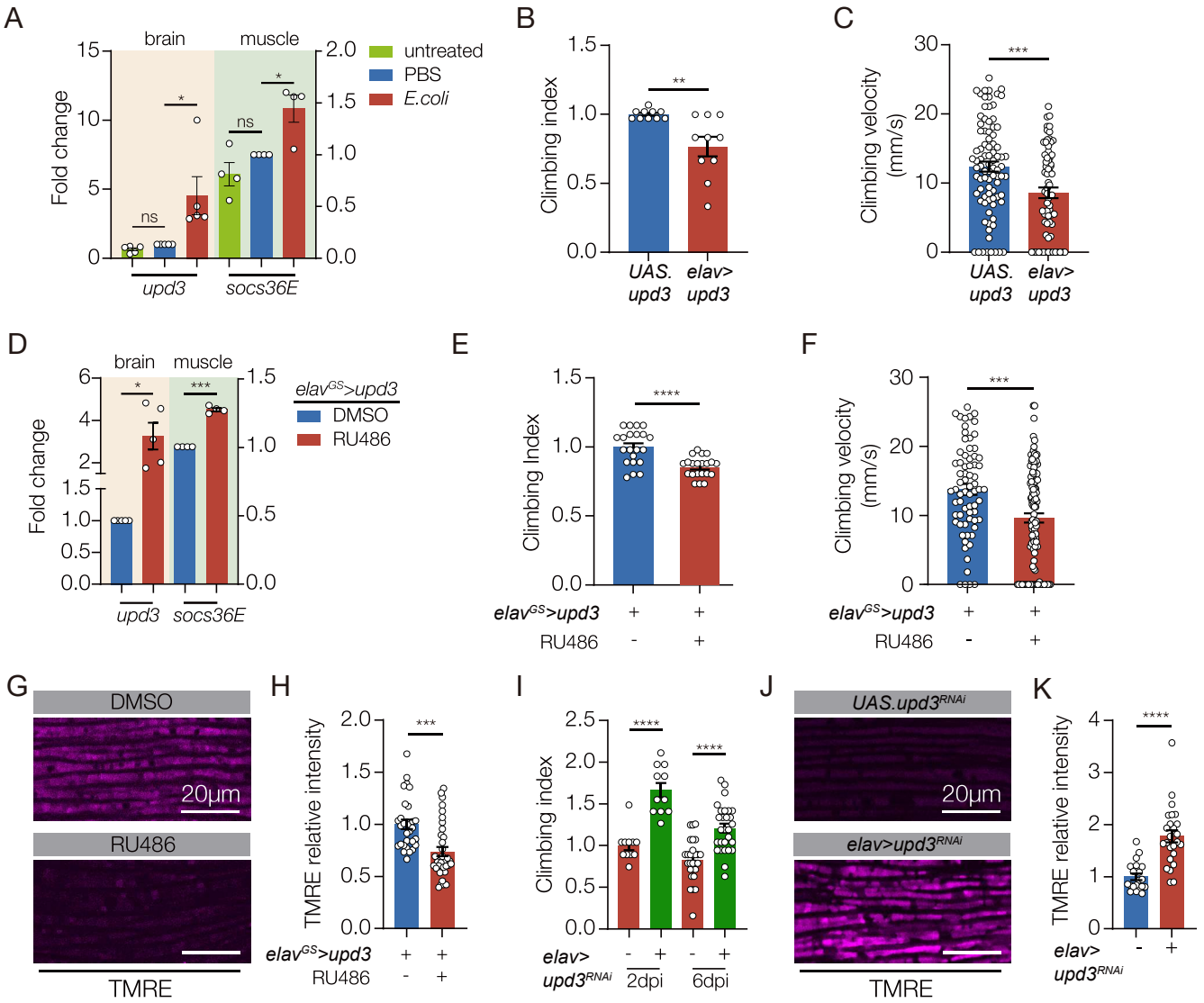

Figure 2. Neuroinflammation activates a Upd3 brain-muscle signaling axis A. qRT-PCR. Untreated and sterile-injected control flies expressed less *upd3* in the brain and less *socs36e* in indirect flight muscles than *E. coli* injected flies at 7 days post injection (dpi). **B.** Climbing index. *elav>upd3* flies showed reduced climbing capacity compared to controls (*UAS.upd3*). **C.** Climbing velocity. *elav>upd3* flies climbed slower than controls. **D-G.** *elav^{GS}.Gal4* was activated in adult flies with RU486 to induce *upd3* expression in the CNS. **D.** qRT-PCR. *elav^{GS}>upd3* flies treated with RU486 showed more *upd3* in the brain and more *socs36e* in indirect flight muscles than flies treated with DMSO. **E.** Climbing index. *elav^{GS}>upd3* flies treated with RU486 showed reduced climbing capacity compared to DMSO treated controls. **F.** Climbing velocity. *elav^{GS}>upd3* flies treated with RU486 climbed slower than controls. **G.** Confocal micrographs of indirect flight muscles stained with TMRE (violet) to assess mitochondrial membrane potential. Muscles from *elav^{GS}>upd3* flies treated with RU486 showed less TMRE staining than DMSO treated controls. H Quantification of the TMRE signal shown in G. **I.** Climbing index. *upd3^{RNAi}* was used to knock down Upd3 expression in the CNS of *E. coli* infected flies. Infected flies with reduced Upd3 expression (*elav>upd3^{RNAi}*) showed improved climbing capacity compared to controls at 2- and 6- dpi. **J.** Confocal micrographs of indirect flight muscles stained with TMRE (violet). Infected flies with reduced Upd3 expression (*elav>upd3^{RNAi}*) showed improved mitochondrial membrane potential compared to controls at 6dpi. K. Quantification of the TMRE signal shown in J. Significance was determined by one-way ANOVA (A), two-sided unpaired student's t-test (B-H), and two-way ANOVA (I). For qRT-PCR, data points represent biological replicates, with n≥5 flies per cohort. See Fig. 1 legend for Climbing Index and TMRE data points. Error bars represent SEM. (*) $p< 0.05$, (**) $p< 0.01$, (***) $p< 0.001$, (****) $p < 0.0001$, (ns) non-significant.

Supplemental Figure 2, related to Figure 2

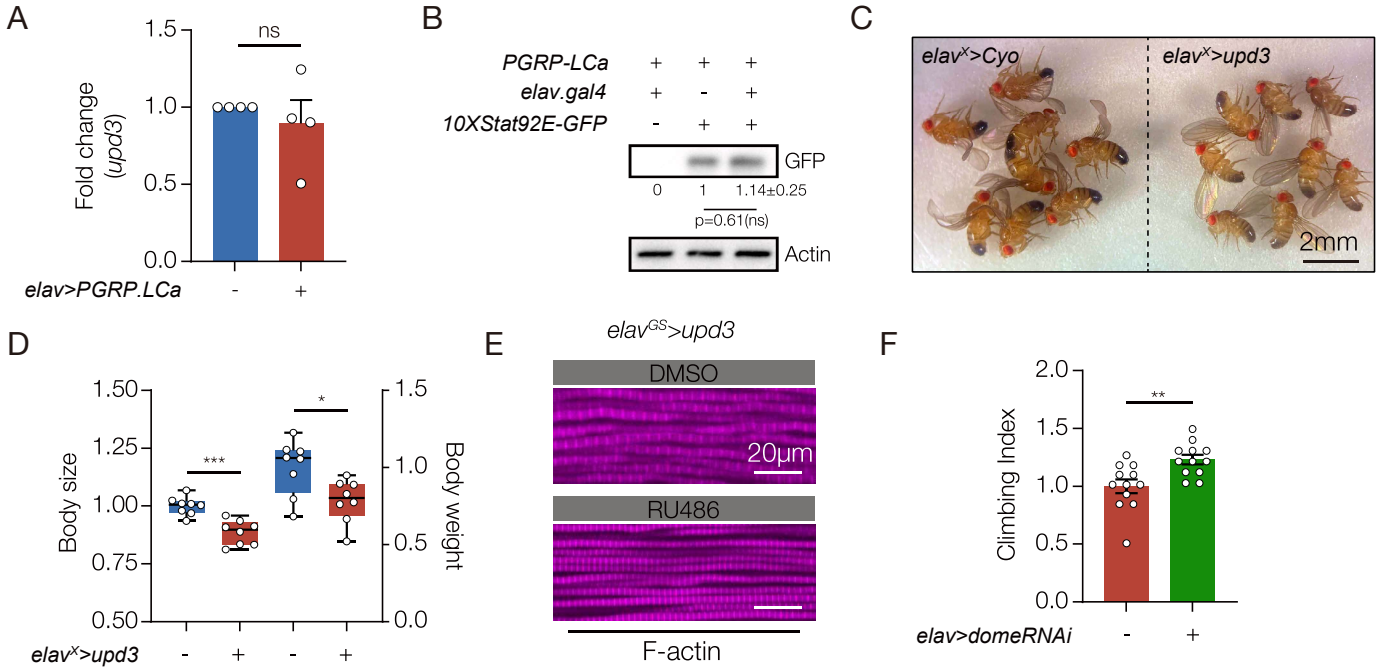

Figure S2. Related to Figure 2. A. qRT-PCR. Flies that expressed PGRP in the CNS (*elav>PGRP.LCa)* showed similar levels of *upd3* mRNA in the brain as control flies. **B.** Western blot. GFP expression from the JAK/Stat activity reporter *10XStat92E.GFP* in muscle was similar between control and *elav>PGRP.LCa* flies. Relative expression was determined for three biological replicates. **C.** Micrographs of adult flies 3-5 days after eclosion. $elav^{X}$*>upd3* flies were smaller than controls. **D.** Normalized body size (left Y axis) and body weight (right Y axis) of control and $elav^{X}$*>upd3* flies. **E.** Confocal micrographs of indirect flight muscles stained with phalloidin to visualize F-actin (violet). $elav^{GS}$*>upd3* flies treated with RU486 or DMSO showed similar myofiber morphology **F.** Climbing index. $dome^{RNAi}$ was used to knock down Dome expression in skeletal muscle of *E. coli* infected flies. Infected flies with reduced Dome expression (*Mef2>dome* ^{RNAi}) showed improved climbing capacity compared to controls at 2 dpi. Significance was determined by two-sided unpaired student's t-test. For qRT-PCR, data points represent biological replicates, with n≥10 flies per cohort. See Fig. 1 legend for Climbing Index data points. Error bars represent SEM. (*) $p< 0.05$, (**) $p< 0.01$, (***) $p< 0.001$, (****) $p < 0.0001$, (ns) non-significant.

Figure 3. ORF3a is expressed in the brain of COVID-19 patients

A

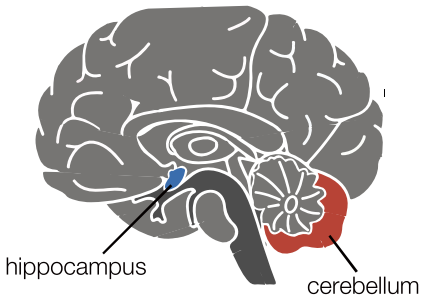

B

Patient	Cerebellum	Hippocampus
P1	+	+
P2	+	+
P3	+	-
P4	+	-
P5	+	-
P6	+	+

C

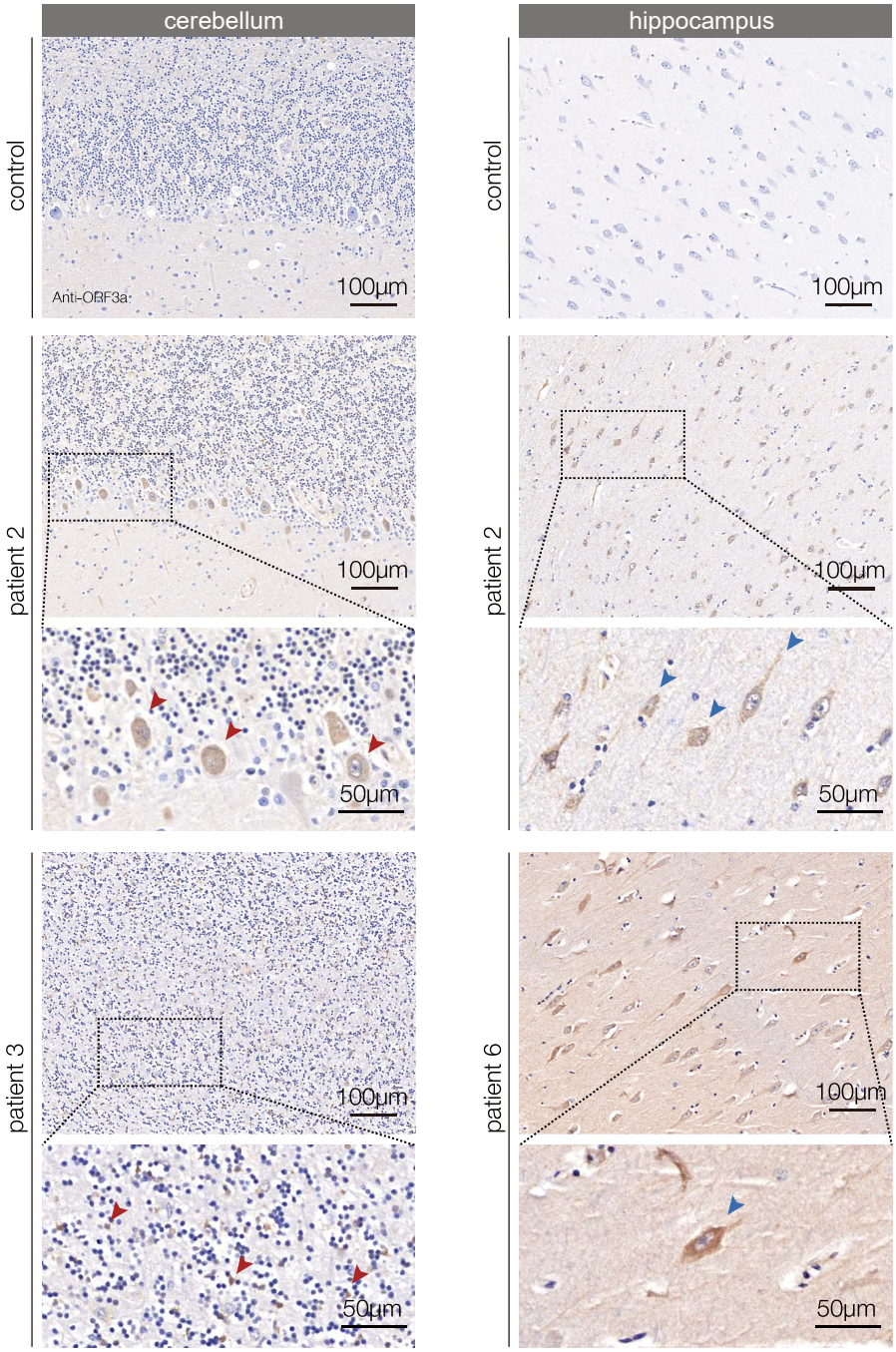

Figure 3. ORF3a is expressed in the brain of COVID-19 patients. A. Diagram of the human brain. **B.** Summary of the histological findings shown in C. The cerebellum and hippocampus samples from COVID-19 patients (patients 2,3 and 6) showed distinct and specific SARS-CoV-2 ORF3a antibody staining. Positive staining was not observed in uninfected controls. **C.** Micrographs of FFPE sections from COVID-19 patients and uninfected patients stained with an ORF3a antibody. In the cerebellum, ORF3a protein (brown) was detected in the plasmalemma and cytolymph of Purkinje cells (patient 2, red arrowheads) and Granular cells (patient 3, red arrows). In the hippocampus ORF3a protein was detected in pyramidal cells in (patients 2 and 6, blue arrowheads).

Figure 4. ORF3a induces neuroinflammation and reduces muscle performance in *Drosophila*

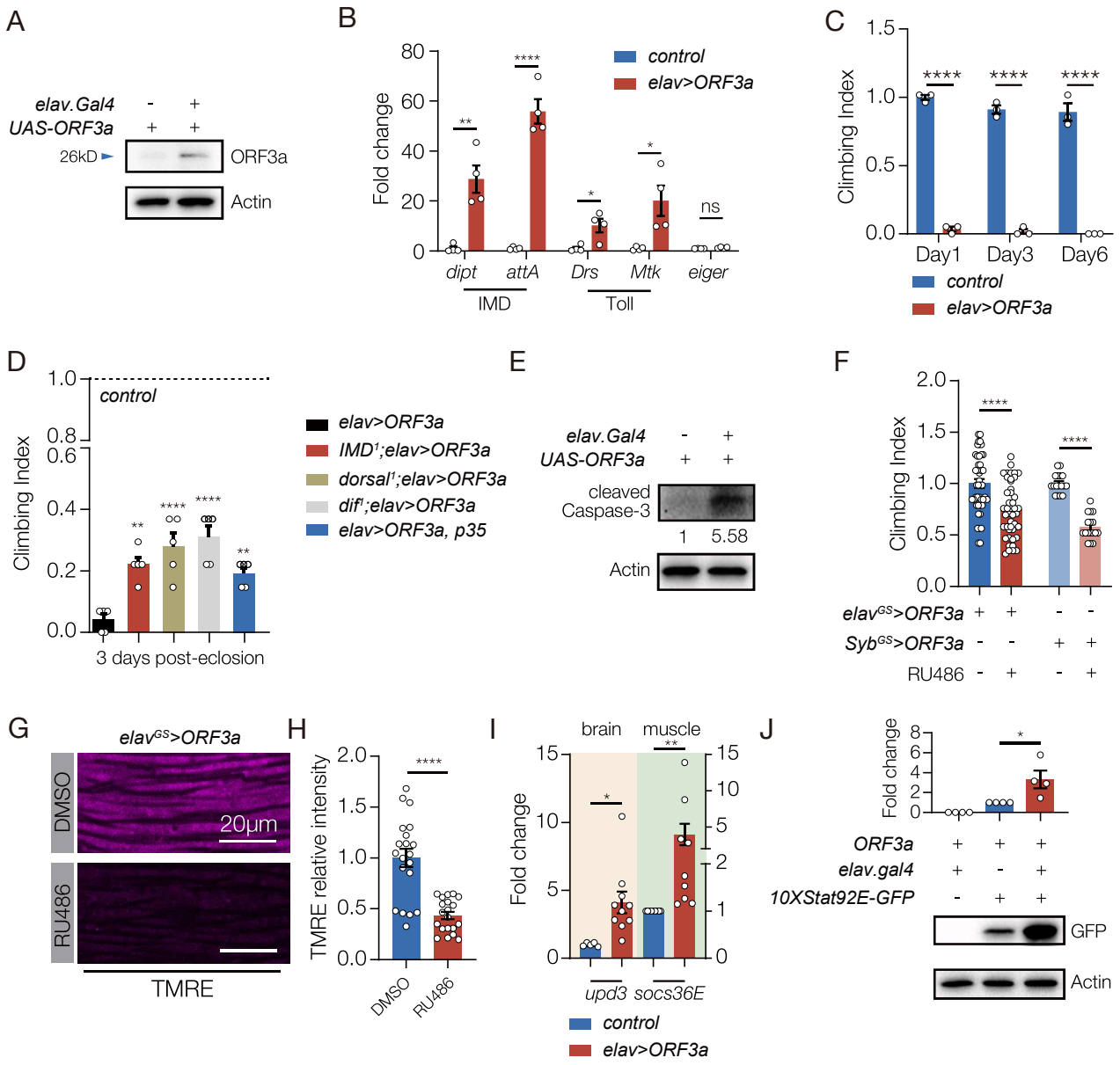

Figure 4 ORF3a induces neuroinflammation and reduces muscle performance in *Drosophila.* **A.** Western blot. ORF3a protein was expressed in the brain of *elav>ORF3a* flies but not in control flies (*UAS.ORF3a*). ORF3a was detected at ~26kD. **B.** qRT-PCR. Transcripts encoding the antimicrobial peptides (AMPs) activated by the IMD pathway (*Dipt* and *attA*) and the Toll pathway (*Drs* and *Mtk*) were enriched in the brain of *elav>ORF3a* flies compared to controls (*UAS.ORF3a*). The cytokine *eiger* is a TNF orthologue that can induce apoptosis in response to infection (Igaki and Miura, 2014), but *eiger* expression was unchanged in *elav>ORF3a* flies. **C.** Climbing index. *elav>ORF3a* flies showed reduced climbing capacity compared to controls (*UAS.ORF3a*) at 1-, 3-, and 6-days after eclosion. **D.** Climbing index. *elav>ORF3a* flies with homozygous mutations affecting the IMD pathway (IMD^1) or the Toll pathway ($dorsal^1$, dif^1) showed improved climbing capacity compared to *elav>ORF3a* flies. *elav>ORF3a* flies that expressed the inhibitor of apoptosis p35 in the CNS also showed im-proved climbing capacity compared to *elav>ORF3a* flies. Control flies (*UAS.ORF3a*) were used to establish the base of the index. **E.** Western blot. Cleaved Caspase-3 was enriched in the brain of *elav>ORF3a* flies compared to controls (*UAS.ORF3a*). **F,G.** $elav^{GS}.Gal4$ and $Syb^{GS}.Gal4$ were activated in adult flies with RU486 to induce *ORF3a* expression in the CNS. **F.** Climbing index. $elav^{GS}$*>ORF3a* and Syb^{GS}*.ORF3a* flies treated with RU486 showed re-duced climbing capacity compared to DMSO treated controls. **G.** Confocal micrographs of indirect flight muscles stained with TMRE (violet) to assess mitochondrial membrane poten-tial. Muscles from $elav^{GS}$*>ORF3a* flies treated with RU486 showed less TMRE staining than DMSO treated controls. H. Quantification of the TMRE signal shown in G. **I.** qRT-PCR. *elav>ORF3a* flies expressed more *upd3* in the brain and more *socs36e* in indirect flight mus-cles than control flies (*UAS.ORF3a*) at 7 days after eclosion. **J.** Western blot. GFP expression from the JAK/Stat activity reporter *10XStat92E.GFP* in muscle was enriched in *elav>ORF3a* flies compared to controls (*UAS.ORF3a*). Significance was determined by two-sided unpaired Student's t-test (F, H, I, J), two-way ANOVA (B, C), and one-way ANOVA (D). For Western blots and qRT-PCR, relative expression was determined for three biological replicates. See Fig. 1 legend for Climbing Index data points. Error bars represent SEM. (*) $p< 0.05$, (**) $p< 0.01$, (***) $p< 0.001$, (****) $p < 0.0001$, (ns) non-significant.

Supplemental Figure 3, related to Figure 4

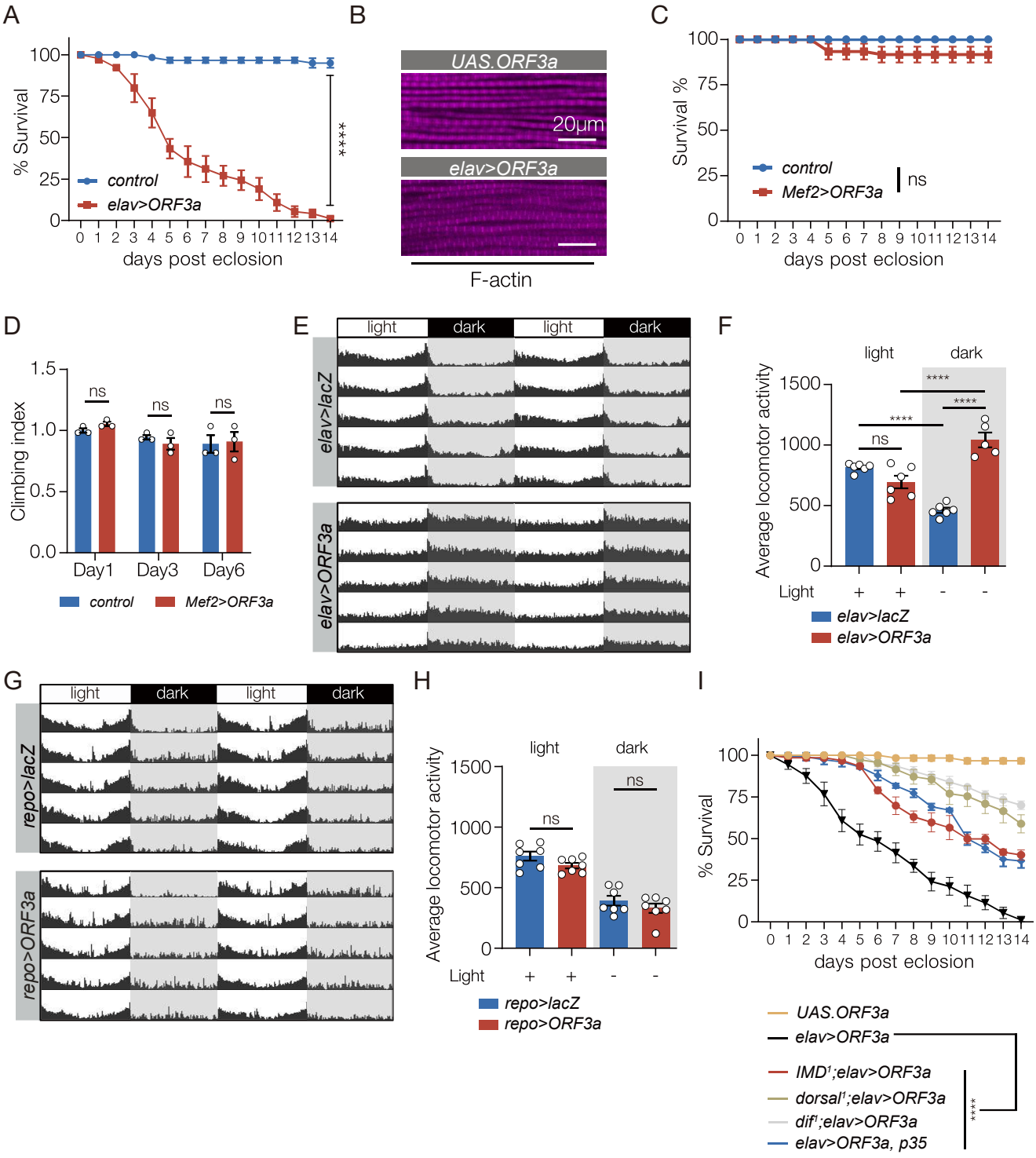

Figure S3 Related to Figure 4.

A. Survival curves. *elav>ORF3a* flies showed a significant reduction in longevity compared to control flies (*UAS.ORF3a*). n=5 cohorts per genotype, with n≥20 flies per cohort. **B.** Confocal micrographs of indirect flight muscles stained with phalloidin to visualize F-actin (violet). *elav>ORF3a* flies and control flies (*UAS.ORF3a*) showed similar myofiber morphology. **C.** Survival curve. *Mef2>ORF3a* flies and control flies (*UAS.ORF3a*) showed comparable longevity. n=3 cohorts per genotype, with n≥20 flies per cohort. **D.** Climbing index. *Mef2>ORF3a* flies showed and control flies (*UAS.ORF3a*) showed similar climbing capacity at 1-, 3-, and 6-days after eclosion. **E,G.** Actograms. Average activity of flies over 2-days is shown. **E.** Flies that expressed ORF3a broadly in the CNS (*elav>ORF3a*) flies were more active in dark cycles than control flies (*elav>lacZ*). **F.** Quantification of data shown in E. n = 28 flies per each genotype. **G.** Flies that expressed ORF3a only in glial cells (*repo>ORF3a*) flies showed similar activity in light and dark cycles as control flies (*repo>lacZ*). **H.** Quantification of data shown in G. n = 16 flies per each genotype. **I.** Survival curves. *elav>ORF3a* flies with homozygous mutations affecting the IMD pathway (IMD^1) or the Toll pathway ($dorsal^1$, dif^1) showed improved longevity compared to *elav>ORF3a* flies. *elav>ORF3a* flies that expressed the inhibitor of apoptosis p35 in the CNS also showed improved longevity compared to *elav>ORF3a* flies. n=3 cohorts per genotype, with n≥20 flies per cohort. Significance was determined by Kaplan–Meier test (A, C, I), and two-way ANOVA (D, F, H). Data represent the average of at least three independent tests. Error bars represent SEM. (****) $p < 0.0001$, (ns) not significant.

Figure 5. ORF3a enhances ROS in the brain and reducesmitochondrial function in skeletal muscle

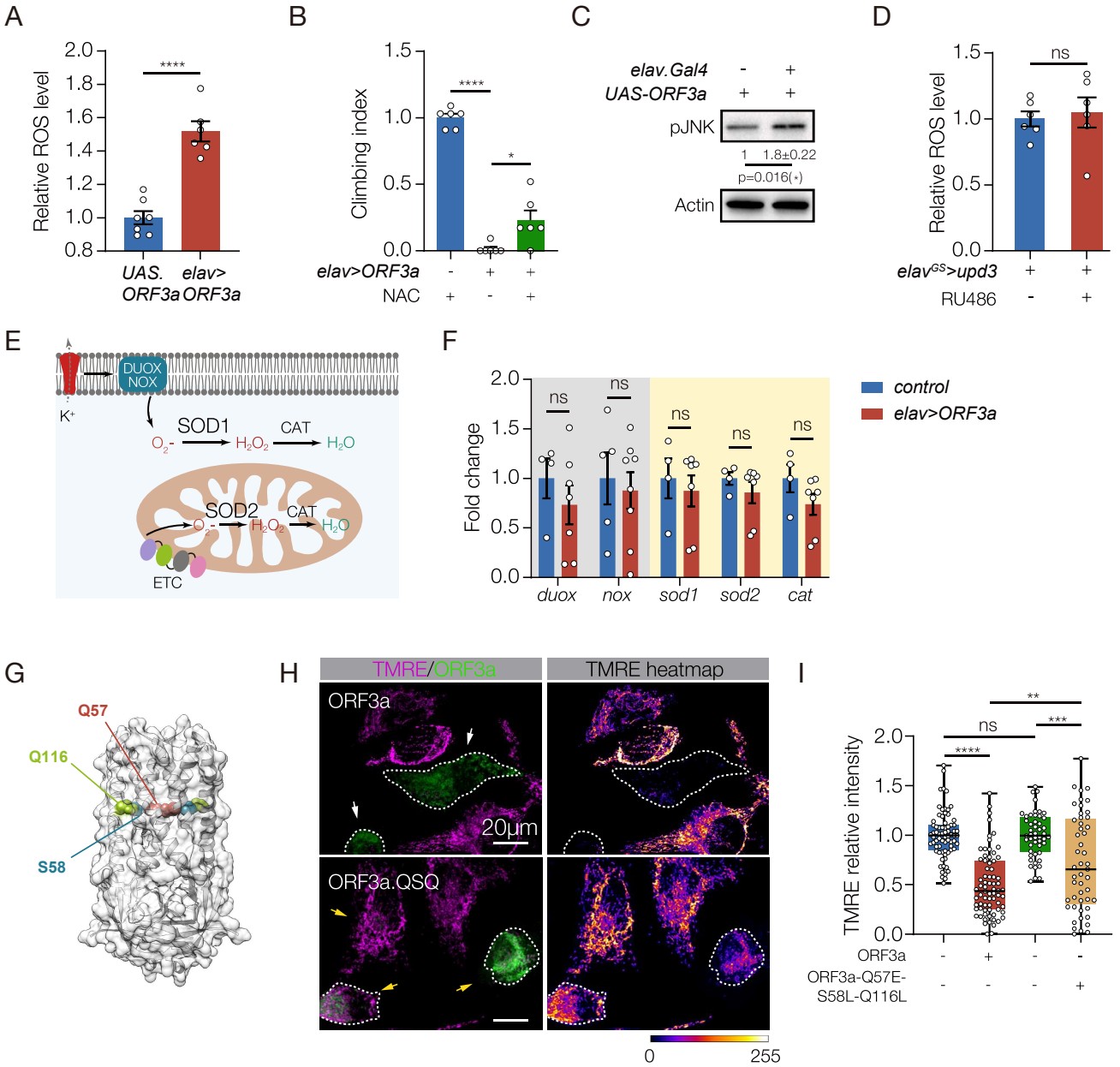

Figure 5 ORF3a enhances ROS in the brain and reduces mitochondrial function in skeletal muscle. A. ROS assay. H2DCFDA was used to measure ROS in the brain. *elav>ORF3a* flies produced more ROS than controls (*UAS.ORF3a*). **B.** Climbing index. *elav>ORF3a* flies treated with the ROS inhibitor N-acetyl-L-cysteine (NAC) showed improved climbing capacity compared to vehicle-treated controls. Wild-type flies treated with NAC were used to establish the base of the index. **C.** Western blot. pJNK levels in the brain were enriched in *elav>ORF3a* flies compared to controls (*UAS.ORF3a*). **D.** ROS assay. *elav*^{GS}*>upd3* flies treated with RU486 accumulated more ROS in the brain than DMSO treated controls. **E.** Diagram of canonical ROS pathways. **F.** qRT-PCR. The expression of ROS-related transcripts in the brain was comparable between *elav>ORF3a* and control (*UAS.ORF3a*) flies. **G.** Cryo-EM structure of the ORF3a dimer, modified from (Kern et al., 2021). Residues positioned at the top of the polar cavity (Q57) or at the base of the hydrophilic grooves (S58, Q116) are shown. **H.** Micrographs of HeLA cells transfected with eGFP.ORF3a or triple mutant eGFP.ORF3a.QSQ (Q57E, S58L, Q116L), labeled for GFP (green) and TMRE (violet) to measure mitochondrial membrane potential. Cells transfected with wild-type ORF3a showed less TMRE fluorescence than cells transfected with ORF3a.QSQ. Dotted lines outline transfected cells. **I.** Quantification of TMRE fluorescence shown in H. Significance was determined by two-sided unpaired student's t-test (A, C, D, F), and one-way ANOVA (B, I). For Western blots, qRT-PCR, and ROS assays relative expression was determined for a minimum of three biological replicates. See Fig. 1 legend for Climbing Index data points. Data points for TMRE expression represent fluorescence in a single transfected cell normalized to untransfected cells within the same field. n=10 fields. Error bars represent SEM. (*) $p < 0.05$, (**) $p < 0.01$, (***) $p < 0.001$, (****) $p < 0.0001$, (ns) non-significant.

Supplemental Figure 4, related to Figure 5

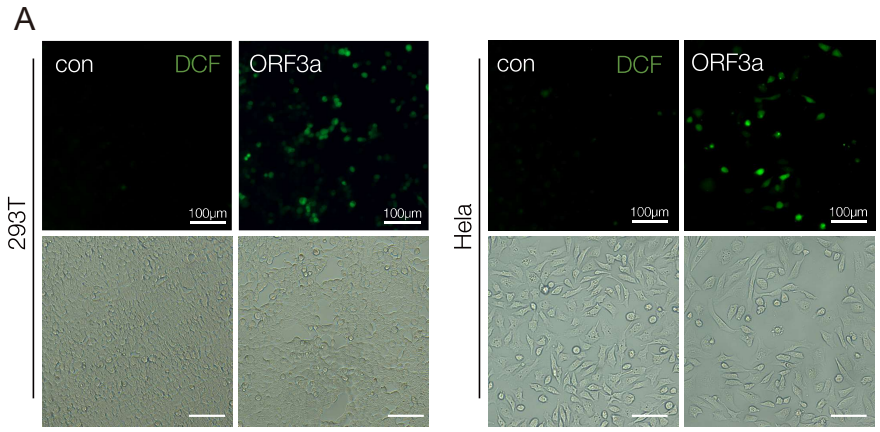

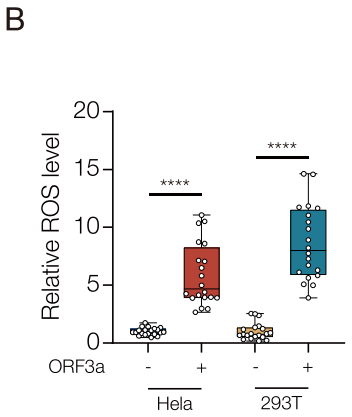

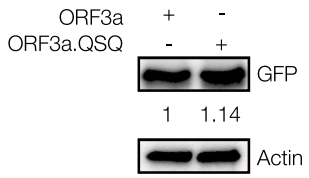

Figure S4 Related to Figure 5.

A. ROS assay. H2DCFDA was used to measure ROS in cultured cells. Micrographs of DCF fluorescence (green) in HEK293T cells (left) and HeLa cells (right) transfected with wild-type ORF3a. ORF3a transfected cells produced more ROS than untransfected controls. **B.** Quantification of ROS levels shown in A. Data points represent fluorescence in a single cell normalized to control cells. n=5 fields **C.** Western blot. HEK293T cells transfected with wild-type ORF3a and ORF3a.QSQ showed similar levels of ORF3a protein expression. Significance was determined by two-sided unpaired student's t-test (B). Error bars represent SEM. (****) $p < 0.0001$.

Figure 6. ORF3a induces neuroinflammation and reduces muscle performance in mice.

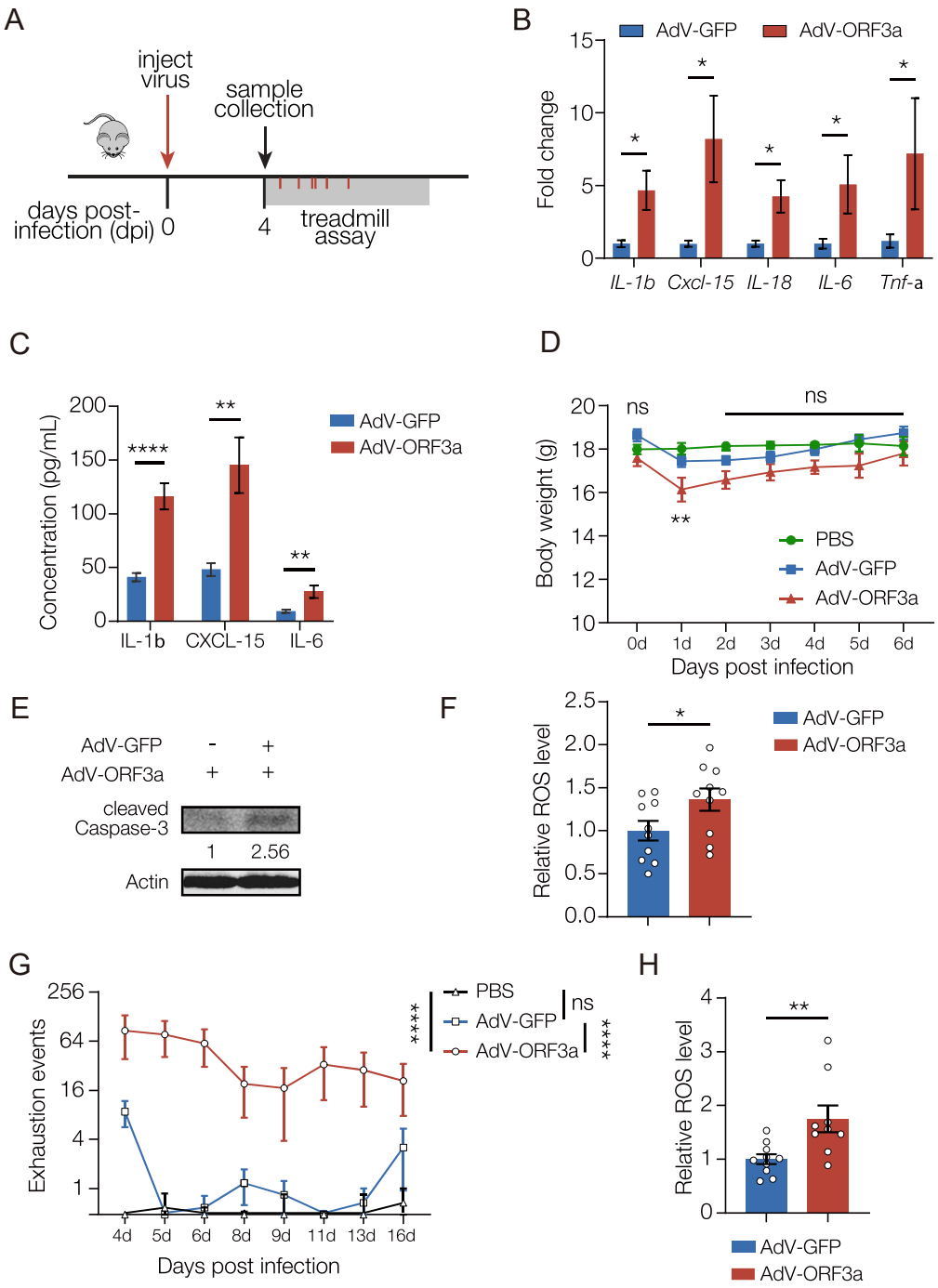

Figure 6 ORF3a induces neuroinflammation and reduces muscle performance in mice. **A.** Experimental design to study the skeletal muscle response to ORF3a expression in mice. **B.** qRT-PCR. Transcripts encoding cytokines were enriched in the brain of AdV-ORF3a.GFP infected mice compared to AdV-GFP infected controls. n≥5. **C.** Enzyme-linked immunosorbent assay (ELISA). Cytokine protein levels were enriched in in the brain of AdV-ORF3a.GFP infected mice compared to AdV-GFP infected controls. n≥5. **D.** Body weight changes over time. Mice infected with AdV-ORF3a.GFP showed a temporary drop in body weight at 1dpi compared to PBS injected or AdV-GFP injected controls. n=6. **E.** Western blot. GFP-positive brain lysates from AdV-ORF3a.GFP infected mice contained more cleaved Caspase-3 than AdV-GFP infected mice. **F.** ROS assay. H2DCFDA was used to measure ROS levels in GFP-positive brain tissue. AdV-ORF3a.GFP infected mice produced more ROS than AdV-GFP infected mice. Each data point represents an individual mouse. **G.** Longitudinal forced treadmill-running assay. AdV-ORF3a.GFP infected mice showed more exhaustion events than AdV-GFP infected mice or PBS injected mice. n≥11. **H.** ROS assay. H2DCFDA was used to measure ROS levels in skeletal muscle. AdV-ORF3a.GFP infected mice produced more ROS than AdV-GFP infected mice. Each data point represents an individual mouse. Significance was determined by two-sided unpaired Student's t-test (B, C, F, H), and one-way ANOVA (D, G). Error bars represent SEM. (*) $p < 0.05$, (**) $p < 0.01$, (****) $p < 0.0001$, (ns) non-significant.

Supplemental Figure 5, related to Figure 6

A

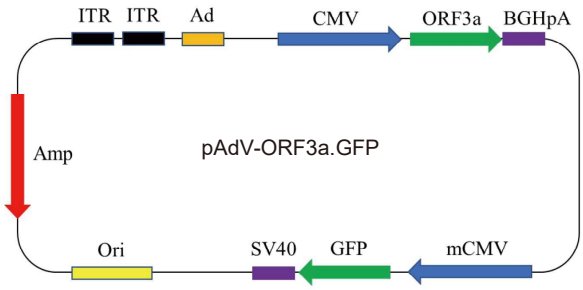

B

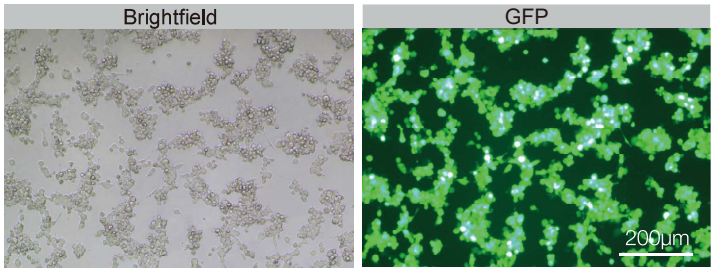

C

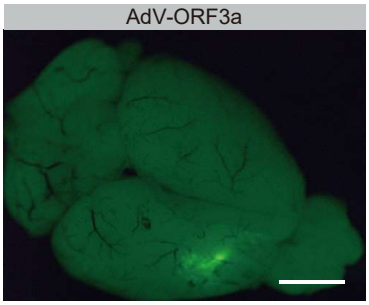

Figure S5 Related to Figure 6.

A. Vector map of AdV-ORF3a.GFP. **B.** Micrograph of HEK293 cells transduced with AdV-ORF3a.GFP. Transduced cells expressed ORF3a.GFP. **C.** Micrograph of a whole mount brain after retro-orbital injection of AdV-ORF3a.GFP. Transduced neural tissue expressed ORF3a.GFP.

Figure 7. The brain-muscle axis is activated in a *Drosophila* model of AD

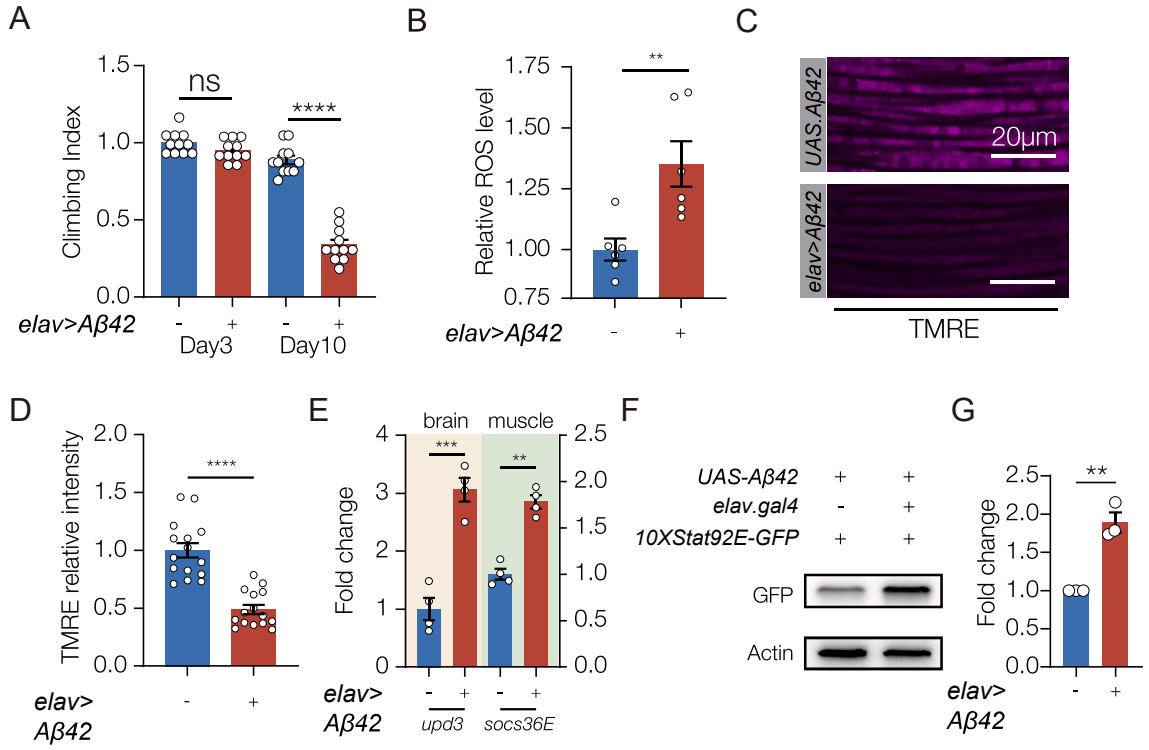

Figure 7. The brain-muscle axis is activated in a *Drosophila* model of Alzheimer's disease (AD). A. Climbing index. Flies that expressed the AD-associated protein *Aβ42* in the CNS (*elav>Aβ42*) showed reduced climbing capacity compared to controls (*UAS.Aβ42*) 10 days after eclosion. **B.** ROS assay. H2DCFDA was used to measure ROS in the brain. *elav> Aβ42* flies produced more ROS than controls (*UAS.Aβ42*). **C.** Confocal micrographs of indirect flight muscles stained with TMRE (violet) to assess mitochondrial membrane potential. Muscles from *elav>Aβ42* flies showed less TMRE staining than controls (*UAS.Aβ42*). **D.** Quantification of mitochondrial membrane potential shown in C. **E.** qRT-PCR. *elav>Aβ42* flies expressed more *upd3* in the brain and more *socs36e* in indirect flight muscles than control flies (*UAS.Aβ42*). **F.** Western blot. GFP expression from the JAK/Stat activity reporter *10XStat92E.GFP* in muscle was enriched in *elav>Aβ42* flies compared to controls (*UAS.Aβ 42*). **G.** Quantification of GFP expression shown F. Experiments in B-G were performed on 10 day old flies. Significance was determined by one-way ANOVA (A), and two-sided unpaired Student's t-test (B, D, F, H). For Western blots, qRT-PCR, and ROS assays relative expression was determined for a minimum of three biological replicates. See Fig. 1 legend for Climbing Index and TMRE data points. Error bars represent SEM. (**) $p < 0.01$, (***) $p < 0.001$, (****) $p < 0.0001$, (ns) non-significant.

Supplemental Figure 6, related to Figure 7

A

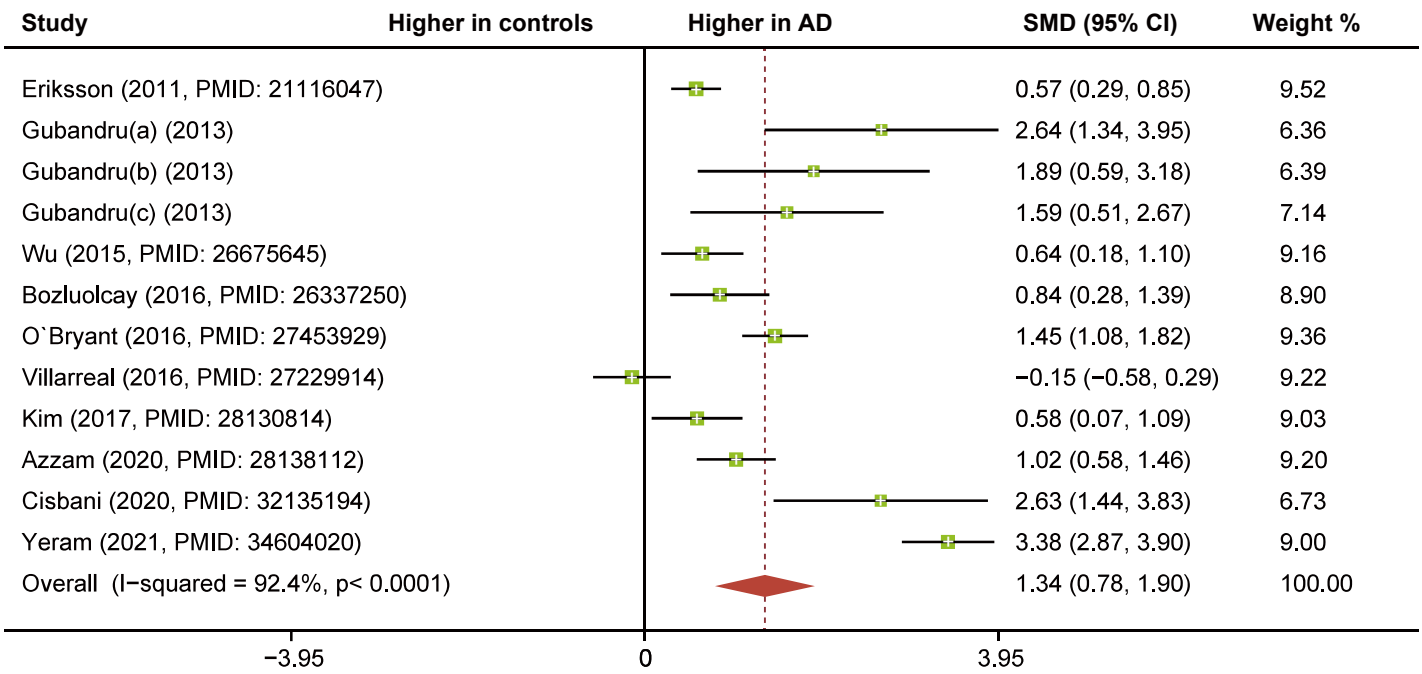

NOTE: Weights are from random effects analysis

B

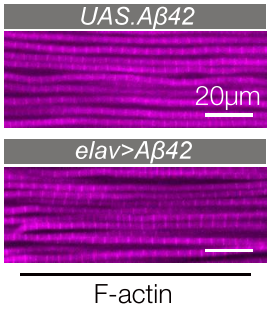

Figure S6 Related to Figure 7.

A. Forest plot depicting IL-6 levels in AD patients. Squares represent the odds ratio and horizontal lines show the 95% confidence intervals. The solid vertical line corresponds to no effect. The red diamond shows the summary measure, indicating the serum levels of IL-6 were increased in AD patients (n=585) compared to health controls (n=439). **B.** Confocal micrographs of indirect flight muscle stained with phalloidin to visualize F-actin (violet). Muscle morphology was comparable between control (*elav>Gal4*) and *elav>Aβ42* flies.